Molecular Cell

Article

# A liquid-like coat mediates chromosome clustering during mitotic exit

## Graphical abstract

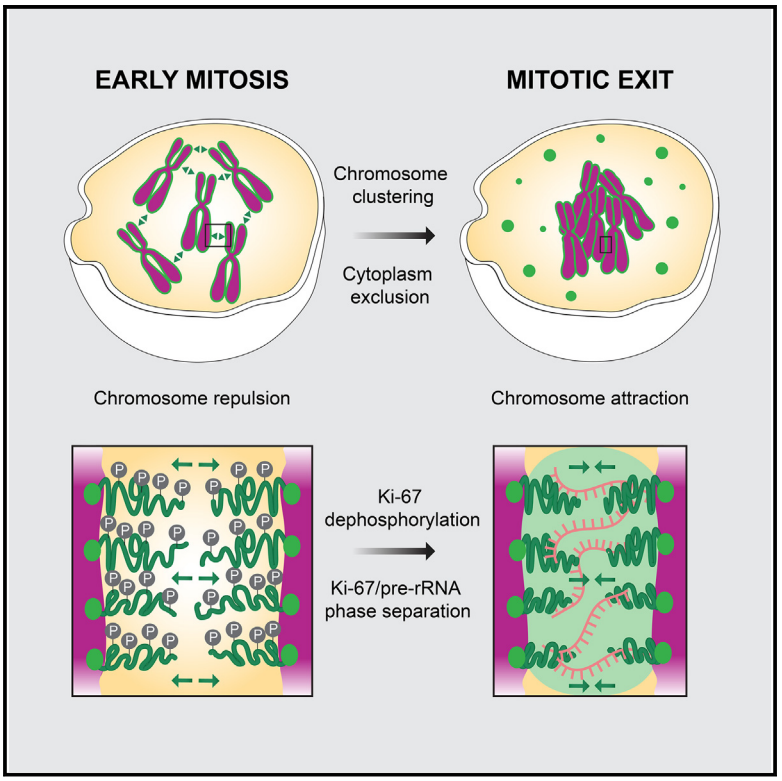


## Authors

Alberto Hernandez-Armendariz, Valerio Sorichetti, Yuki Hayashi, ..., Jan Ellenberg, Anđela Šarić, Sara Cuylen-Haering

## Correspondence

sara.cuylen-haering@embl.de

## In brief

Hernandez-Armendariz et al. show that Ki-67 generates a liquid-like layer with premature ribosomal RNAs on the chromosome surface to promote chromosome clustering during exit from mitosis. The transition of Ki-67 from chromosome repellent to attractant is triggered by a change in its phosphorylation status.

## Highlights

- At anaphase onset, Ki-67 changes its properties upon dephosphorylation
- Ki-67 forms condensates with premature ribosomal RNAs during anaphase
- A charged patch in Ki-67's N terminus is required for condensate formation
- Ki-67/pre-rRNA condensation is required for chromosome clustering

Hernandez-Armendariz et al., 2024, Molecular Cell *84*, 3254–3270
September 5, 2024 
https://doi.org/10.1016/j.molcel.2024.07.022

CellPress

CellPress
OPEN ACCESS

Molecular Cell

Article

# A liquid-like coat mediates chromosome clustering during mitotic exit

Alberto Hernandez-Armendariz,[1,2] Valerio Sorichetti,[3] Yuki Hayashi,[1] Zuzana Koskova,[1,2] Andreas Brunner,[1,2] Jan Ellenberg,[1] Anđela Šarić,[3] and Sara Cuylen-Haering[1,4,*]

[1]Cell Biology and Biophysics Unit, European Molecular Biology Laboratory (EMBL), 69117 Heidelberg, Germany
[2]Collaboration for Joint PhD Degree between EMBL and Heidelberg University, Faculty of Biosciences, Heidelberg, Germany
[3]Institute of Science and Technology Austria, 3400 Klosterneuburg, Austria
[4]Lead contact
*Correspondence: sara.cuylen-haering@embl.de
https://doi.org/10.1016/j.molcel.2024.07.022

## SUMMARY

The individualization of chromosomes during early mitosis and their clustering upon exit from cell division are two key transitions that ensure efficient segregation of eukaryotic chromosomes. Both processes are regulated by the surfactant-like protein Ki-67, but how Ki-67 achieves these diametric functions has remained unknown. Here, we report that Ki-67 radically switches from a chromosome repellent to a chromosome attractant during anaphase in human cells. We show that Ki-67 dephosphorylation during mitotic exit and the simultaneous exposure of a conserved basic patch induce the RNA-dependent formation of a liquid-like condensed phase on the chromosome surface. Experiments and coarse-grained simulations support a model in which the coalescence of chromosome surfaces, driven by co-condensation of Ki-67 and RNA, promotes clustering of chromosomes. Our study reveals how the switch of Ki-67 from a surfactant to a liquid-like condensed phase can generate mechanical forces during genome segregation that are required for re-establishing nuclear-cytoplasmic compartmentalization after mitosis.

## INTRODUCTION

Cell division requires a dramatic reorganization of the genome. During entry into mitosis, the formerly loose chromatin fibers compact into dense mitotic chromosomes, built from consecutive chromatin loops that are held together by proteins in a network-like manner.[1] Nuclear envelope breakdown releases mitotic chromosomes into the cytoplasm,[2] and their surface becomes covered by an intricate layer of proteins and ribonucleic acids (RNAs), many of which are otherwise found in the nucleolus during interphase.[3–5] Recent studies have demonstrated that the proliferation marker protein Ki-67 is central to the organization of the chromosome surface since the entire surface layer is delocalized in its absence.[6–8]

During early mitosis, Ki-67 relocalizes from nucleoli to the chromosome surface,[9] where it forms extended brush structures ~90 nm in length.[8] These brushes are thought to mediate the dispersion of individual mitotic chromosomes, facilitating their attachment to mitotic spindle microtubules.[8] Individualized chromosomes are then captured by mitotic spindle microtubules, and once all chromosomes have been bioriented, anaphase segregation is triggered by cleavage of cohesin.[10] During exit from mitosis, the Ki-67 brush structure collapses, and chromosomes cluster in a Ki-67-dependent manner to facilitate the exclusion of large cytoplasmic particles from the future nuclear space.[11] These findings suggest that Ki-67 must fundamentally switch its function between mitotic entry and exit, but the underlying mechanistic basis has remained elusive.

Ki-67 contains several features that have been linked to liquid-liquid phase separation, including structural disorder, low-complexity regions, and multivalency.[12] A recent study[13] reported that single or multiple copies of recombinantly expressed Ki-67 repeats can undergo phase separation *in vitro* at high protein concentrations and in the presence of crowding agents. Phase separation was notably amplified upon phosphorylation, and it has been proposed in this study that phosphorylation plays a pivotal role in Ki-67 phase separation by generating segments with alternating charges within the repeat modules, referred to as "charge blockiness." Since Ki-67 is phosphorylated upon entry into mitosis,[14] it implies that Ki-67 forms a liquid-like layer on the surface of chromosomes during early mitosis. However, direct evidence supporting this hypothesis in living cells is missing, as are insights into the potential significance and relevance of Ki-67 liquid-like properties or its dependency on the cell cycle stage.

Here, we combine quantitative live-cell imaging and protein engineering experiments with coarse-grained simulations to investigate the change of Ki-67's properties through mitosis to understand how chromosomes can completely invert their

 

CellPress
OPEN ACCESS

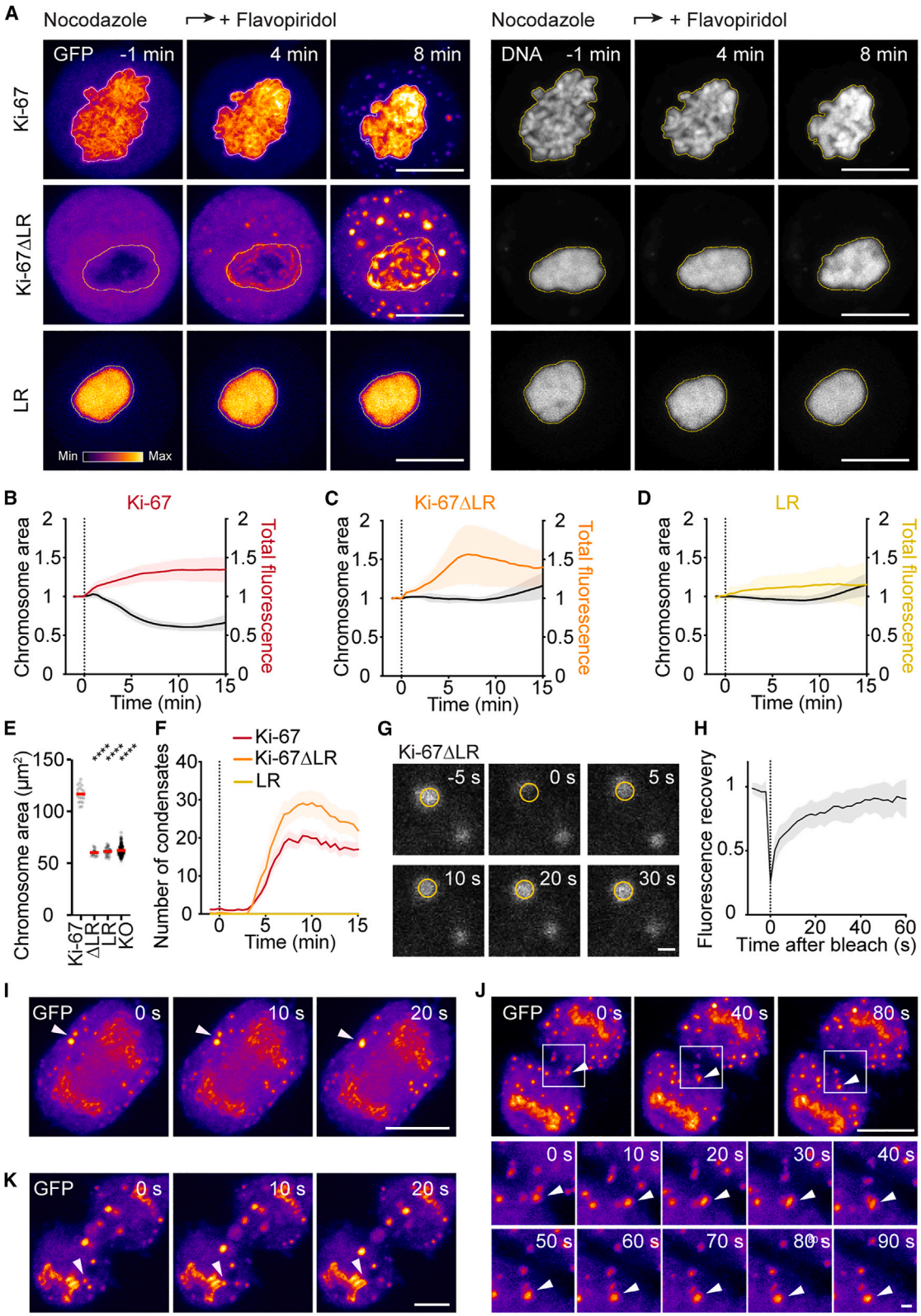


*(legend on next page)*

physical properties. We demonstrate that, upon dephosphorylation at anaphase onset, Ki-67, together with RNA, forms cytoplasmic foci with liquid-like properties, which can fuse with the chromosome-bound pool, suggesting a liquid-like character of the chromosome surface during exit from mitosis. Consequently, chromosome surfaces no longer repulse but instead attract each other, thereby promoting chromosome clustering and the subsequent exclusion of cytoplasm from the newly formed nucleus. This transition of Ki-67 to a condensed state is RNA-dependent and requires a highly positively charged site within the N terminus of Ki-67. Our findings hence illustrate how an acute switch in protein properties from a dispersed to a condensed state can generate large-scale adhesive forces to perform an important cellular function during cell division.

## RESULTS

### Ki-67 changes its properties during mitotic exit

To investigate the properties of Ki-67 during mitosis and unravel their role in chromosome clustering, we utilized a previously established assay that triggers mitotic exit in the absence of a spindle but nevertheless facilitates the timely assembly of a sealed and transport-competent nuclear envelope.[11] This assay relies on first inducing mitotic arrest using nocodazole, which depolymerizes microtubules, followed by triggering mitotic exit through acute inhibition of the mitotic kinase CDK1 using flavopiridol.[15]

As expected, chromosomes clustered within a few minutes after the addition of flavopiridol. Concomitantly, the total signal intensity of chromosome-bound Ki-67 increased (Figures 1A and 1B; Video S1), ruling out the possibility that chromosome clustering is simply triggered by the reduction of the chromosomal fraction of Ki-67. Importantly, the increase in chromosome-bound Ki-67 during anaphase was also evident in a cell line that expresses endogenously tagged Ki-67 (Figures S1A and S1B). Furthermore, FCS-calibrated imaging of unperturbed cells revealed that Ki-67 endogenous concentration on chromosomes increased from ~500 nM in metaphase to 750 nM in anaphase (Figures S1D–S1I).

To investigate the cause of the increase in chromosome-bound Ki-67 during mitotic exit, we tested its dependency on Ki-67's C-terminal DNA-binding domain, known as the leucine/arginine-rich (LR) domain. We separately expressed the LR domain alone and a truncation lacking the LR domain (Ki-67ΔLR), which localizes to the cytoplasm during early mitosis. As expected, neither the Ki-67ΔLR nor the LR construct restored chromosome dispersal during early mitosis in Ki-67 knockout (KO) cells[8] (Figures 1A and 1E). Thus, chromosomes remained in a clustered state with a constant area until their decompaction started approximately 10 min after induction of mitotic exit. However, while the chromosomal levels of the LR domain alone (LR) remained constant (Figures 1A and 1D; Video S1), remarkably, the initially soluble Ki-67ΔLR[16] notably enriched on chromosomes upon mitotic exit (Figures 1A and 1C; Video S1). The observed chromosomal recruitment of Ki-67ΔLR cannot be due to its multimerization with endogenous full-length Ki-67 since the constructs were expressed in Ki-67 KO cells. Furthermore, the increase of Ki-67ΔLR on chromosomes preceded the binding of the DNA-bridging barrier-to-autointegration factor (BAF)[17] and the reformation of the nuclear envelope (Figures S1J–S1L), ruling out that it is a consequence of either of these two events. Our data instead suggests that Ki-67 gains a new DNA-binding activity that is independent of the known LR domain during mitotic exit. Considering that the enrichment of the Ki-67ΔLR construct on chromosomes correlated with chromosome clustering (compare Figures 1B and 1C), it is tempting to speculate that the gain of a second DNA-binding domain might contribute to chromosome clustering by connecting neighboring chromosomes.

Concomitant with Ki-67ΔLR enrichment on mitotic chromosomes, the soluble pool of Ki-67ΔLR formed micron-sized spherical foci (Figures 1A and 1F; Video S1). Full-length Ki-67 formed foci with similar kinetics, reaching peak levels by the time chromosomes were maximally clustered, irrespective of whether it was expressed as a transgene (Figures 1A and 1F) or from the endogenous locus (Figures S1A, S1C, S1G, and S1I). Despite similar kinetics, the number and size of condensates were higher in the ΔLR system. This can be explained by the elevated cytoplasmic concentration due to the initial absence of the chromosome-bound pool, which allows for a robust investigation of condensate properties.

Ki-67ΔLR molecules within foci were highly dynamic, as evidenced by fluorescence recovery within 30 s after photobleaching (Figures 1G and 1H) and the tendency of foci to fuse and relax into larger spherical structures over time (Figure 1I). Furthermore,

**Figure 1. Ki-67 phase separates and enriches on chromosomes as they cluster during mitotic exit**

(A) Time-lapse confocal microscopy of spindle-less mitotic exit of Ki-67 KO with indicated constructs in nocodazole. Flavopiridol added at t = 0 min. DNA labeled with SiR-Hoechst. White and yellow lines represent chromosomal segmentations quantified in (B)–(E).

(B–D) Chromosome ensemble area over time and EGFP total fluorescence intensity in the chromosomal area ($n \geq 18$).

(E) Chromosome ensemble area (before flavopiridol) of Ki-67 KO cells with indicated constructs plotted in (B)–(D). Untransfected Ki-67 KO cells arrested by nocodazole shown for reference ($n \geq 18$).

(F) Quantification of cytoplasmic condensates over time as in (A) ($n \geq 18$).

(G) Photobleaching of condensates in Ki-67 KO cells expressing EGFP-Ki-67ΔLR with fluorescence recovery recorded over time in a circular region (yellow circle). Representative example quantified in (H).

(H) EGFP mean fluorescence intensity in bleached area normalized to pre-bleached values ($n = 13$).

(I) Time-lapse of Ki-67 wild-type cell expressing EGFP-Ki-67ΔLR undergoing anaphase with condensates fusing (white arrows).

(J) Ki-67 KO cell expressing EGFP-Ki-67ΔLR undergoing cytokinesis, zoom-in images below.

(K) Ki-67 wild-type cell expressing Ki-67ΔLR-mNeonGreen, with condensate fusing with the chromosome surface (white arrows).

Dashed lines indicate flavopiridol addition (B–D and F) or photobleaching (H). Red bars indicate mean (E); significance tested versus full-length Ki-67 by two-tailed unpaired t tests (**** $p \leq 1 \times 10^{-15}$). Lines/shaded areas represent mean ± SD (B–D and H) or mean ± SEM (F). Maximum intensity z-projections (A, I, and J) or single z-slices (G and K) shown. Scale bars: 10 μm in (A), (I), (J top), and (K) and 1 μm in (G) and (J bottom).

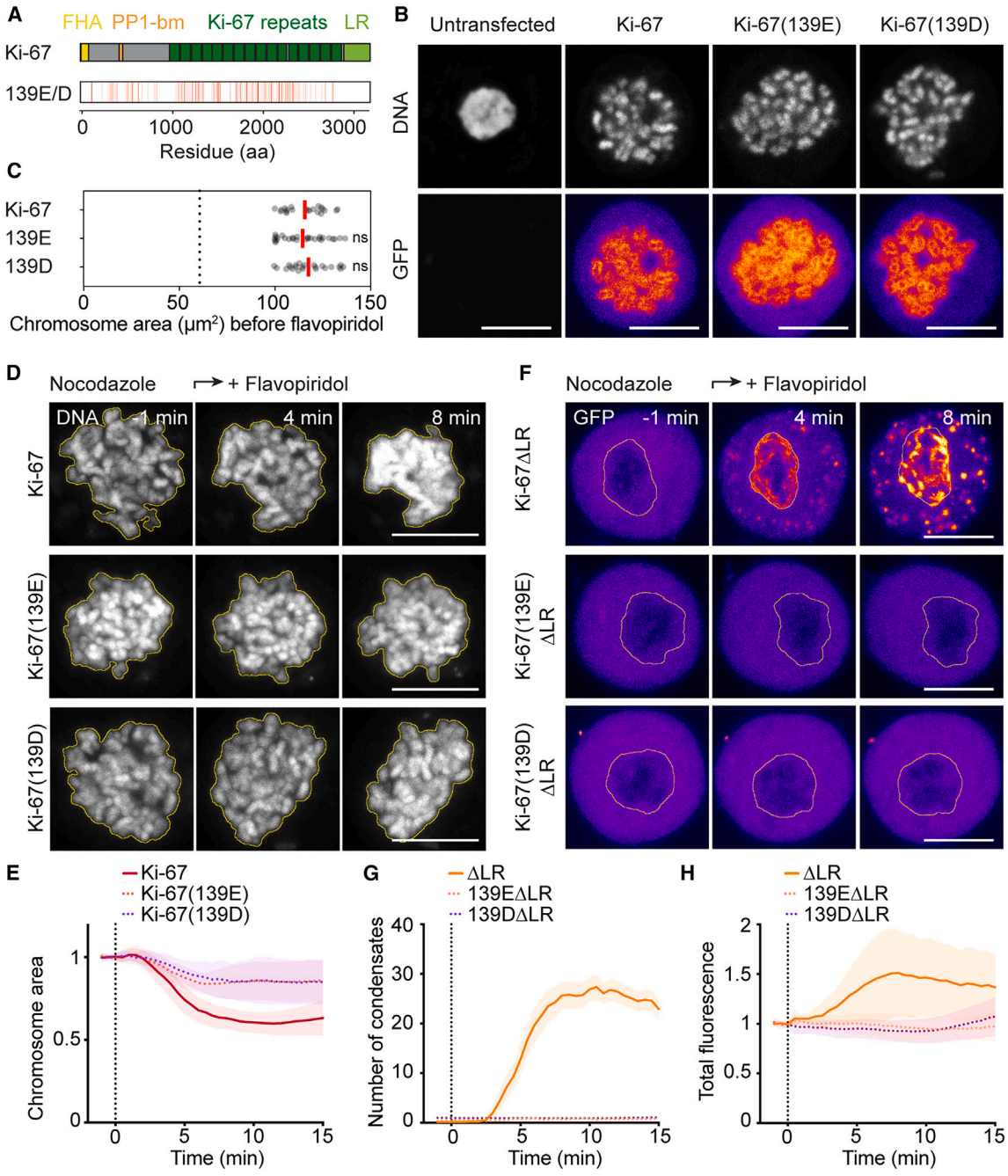


**Figure 2. Ki-67 dephosphorylation controls Ki-67 phase separation, enrichment on chromosomes, and chromosome clustering**

(A) Schematic of Ki-67's domain structure with 139 serine/threonine residues (red lines) substituted to glutamate or aspartate to generate phosphomimetic Ki-67. FHA, fork-head associated domain; PP1-bm, PP1 binding motif; LR, leucine/arginine-rich DNA-binding domain.

(B) Confocal images of Ki-67 KO cells untransfected or expressing indicated constructs arrested by nocodazole in early mitosis.

(C) Initial chromosome ensemble area (before flavopiridol) of Ki-67 KO cells with indicated constructs, plotted in (E). Dashed line indicates mean area of untransfected Ki-67 KO cells from Figure 1E for reference.

(D) Time-lapse of Ki-67 KO cells expressing indicated constructs undergoing spindle-less mitotic exit. Yellow lines represent chromosomal regions used for quantifications in (E).

(E) Chromosome ensemble area over time as in (D) ($n \geq 21$).

*(legend continued on next page)*

Ki-67ΔLR foci located in the cleavage furrow during cytokinesis deformed due to mechanical stress but rounded up again after relaxation (Figure 1J). In addition, cytoplasmic Ki-67ΔLR foci not only fused with each other (Figure 1I) but also with the chromosome-bound pool of Ki-67ΔLR (Figure 1K; Video S2). These findings, along with the high mobility of full-length Ki-67 molecules on the chromosome surface during mitotic exit (Figures S1M and S1N; Saiwaki et al.[18]), suggest that both the chromosome surface and the cytoplasmic pools of Ki-67 gain liquid-like properties during mitotic exit. Chromosome clustering could thus be driven by a transition of Ki-67 into a liquid-like protein layer, by chromosome bridging through the formation of a second DNA-binding site, or by a combination of both mechanisms.

## A phospho-switch controls chromosome clustering

Although Ki-67 gets highly phosphorylated during early mitosis[14] at more than one hundred identified sites,[19] its phosphorylation is largely reverted by the end of anaphase,[18,20] possibly through recruitment of protein phosphatase 1 (PP1).[6] To test whether dephosphorylation triggers the increase of Ki-67 on chromosomes and the change in its phase-separation properties, we generated phosphomimetic versions of Ki-67 by substituting 139 of the serine or threonine residues that had been reported to be phosphorylated[19] for glutamate (Ki-67(139E)) or aspartate (Ki-67(139D)) residues (Figure 2A).

Full-length Ki-67(139E) and Ki-67(139D) localized to the surface of mitotic chromosomes and restored chromosome dispersal during early mitosis in Ki-67 KO cells, as evidenced by a clear separation of individual chromosomes as opposed to a single coalesced structure in untransfected Ki-67 KO cells (Figure 2B). Mitotic chromosome ensemble areas of the phosphomimetic versions reached values comparable to wild-type Ki-67 in early mitosis (Figure 2C), confirming that the mutations did not affect the surfactant function of Ki-67. Expression of Ki-67(139E) or Ki-67(139D) in Ki-67 KO cells, by contrast, strongly reduced chromosome clustering upon exit from mitosis (Figures 2D and 2E; Video S3). To test whether this might be due to a failure of the mutant proteins to enrich and form a condensed phase on the chromosome surface at mitotic exit, we use the robust ΔLR system to quantify condensate formation and enrichment to chromosomes. Indeed, the phosphomimetic versions that lack the LR DNA-binding domain (Ki-67(139E)ΔLR and Ki-67(139D)ΔLR) neither accumulated on chromosomes nor formed condensates in the cytoplasm during exit from mitosis, in contrast to wild-type Ki-67ΔLR (Figures 2F–2H; Video S4).

In summary, our findings, based on phosphomimetic Ki-67 versions, suggest that Ki-67 dephosphorylation upon mitotic exit triggers chromosome clustering, Ki-67 condensate formation, and its enrichment on chromosomes.

## The basic patch of Ki-67 mediates chromosome clustering

To gain further insights into the mechanism of Ki-67 enrichment on chromosomes and its condensate formation ability, we mapped the domains of Ki-67 that are required for either of these two properties. In our initial experiment, we observed that the LR domain alone did not enrich on chromosomes (Figure 1D) and did not form condensates (Figure 1F). Additionally, replacing the LR domain with histone 2B as an alternative means to localize the protein to DNA did not affect chromosome clustering (Figures S2A–S2D), which suggests that the LR domain makes no specific contribution to the clustering function beyond merely anchoring Ki-67 to chromosomes.

We next split the remaining protein sequence of Ki-67 into an N-terminal segment that precedes the Ki-67 repeat motifs (N terminus) and a C-terminal segment that contains the sixteen repeat motifs (C terminusΔLR; Figure 3A). Only the N-terminal segment bound to chromosomes with kinetics similar to Ki-67ΔLR and could form cytoplasmic foci (Figures 3B–3D; Video S5). Chromosomal enrichment of the C-terminal Ki-67 segment started, by contrast, only ∼5 min after induction of mitotic exit, at a time point when chromosome clustering had already largely completed (Figures 1A and 1B). Furthermore, the C-terminal segment did not form condensates, even when highly overexpressed (Figure S3). These results suggest that the ability of Ki-67 to form condensates is encoded in its N-terminal segment.

The N-terminal segment contains two low-complexity regions[21]: one that is present in only one of the two Ki-67 splice isoforms (fragment absent in the short isoform, FASI)[22] and one that is located close to a positively charged patch (CP) of 186 amino acids (Figure 3A). Removal of the CP but not the removal of the FASI (Figures 3B–3D and S3; Video S5) prevented both enrichment on chromosomes and condensate formation of the N-terminal segment during mitotic exit.

Consistent with the notion that the positively CP within the N terminus of Ki-67 is required for Ki-67 enrichment on chromosomes and phase separation, deletion of either the entire N-terminal segment or specifically of the CP from full-length Ki-67 considerably impaired chromosome clustering (Figures 3E, 3F, and S2F; Video S6). Deletion of the Ki-67 repeat domain or the FASI had, by contrast, no effect on the extent of chromosome clustering (Figures 3E, 3F, and S2F). Furthermore, a minimal construct composed of CP-repeats-LR clustered chromosomes to the same extent as wild-type Ki-67 (Figures S2E–S2G). Hence, the N-terminal positively CP is necessary for chromosome clustering.

(F) Time-lapse of Ki-67 KO cells expressing indicated constructs undergoing spindle-less mitotic exit. White lines represent chromosomal regions used for quantifications in (G).
(G) Quantification of cytoplasmic condensates over time as in (F) ($n \geq 23$).
(H) EGFP total fluorescence intensity in segmented chromosome areas over time as in (F) ($n \geq 23$).
Dashed lines indicate flavopiridol addition (E, G, and H). Red bars indicate mean (C); significance tested by two-tailed unpaired t test (Ki-67(139), ns $p = 0.75$; Ki-67(139D), ns $p = 0.54$).
Lines/shaded areas represent mean ± SD (E and H) or mean ± SEM (G). Single z-slices (B) or max. intensity z-projections (D and F) shown. DNA labeled with SiR-Hoechst. Scale bars: 10 μm in (B), (D), and (F).

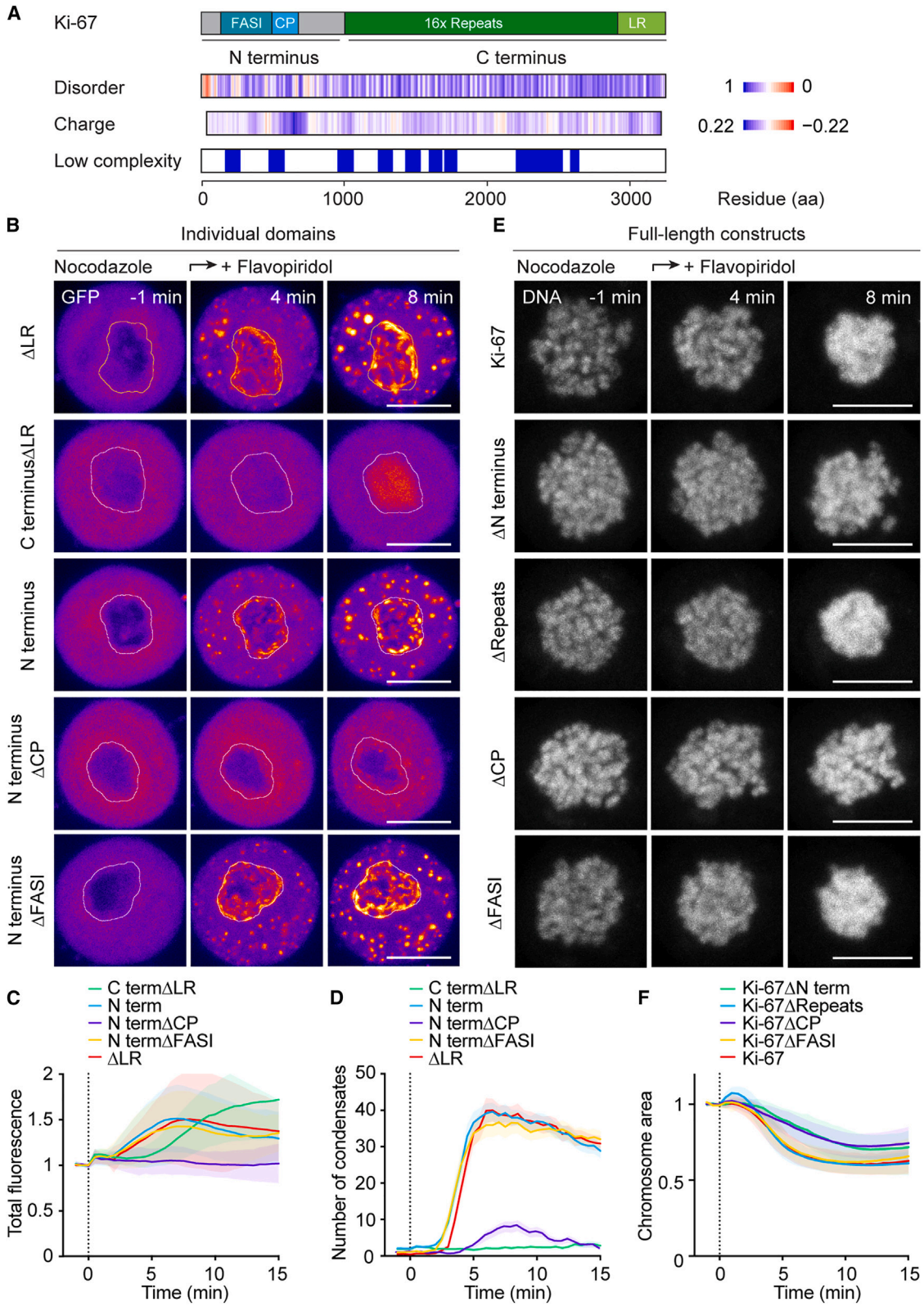


*(legend on next page)*

### The high positive charge is the key feature of the CP

To further investigate how the CP drives chromosome clustering, we tested the relevance of the PP1-binding site and the high positive charge within the CP (Figures 4A and 4B). Both features are evolutionary conserved (Booth et al.[6]; Figure 4B). Mutation of the PP1-binding sequence RVSF to RASA[6] resulted in a slight delay in Ki-67 enrichment on chromosomes, condensate formation, and chromosome clustering (Figure S4). These findings are consistent with the notion that dephosphorylation is critical for the switch in Ki-67 properties upon mitotic exit (Figure 2) and that PP1 contributes to its dephosphorylation.

Mutation of all 37 arginine and lysine residues within the CP to alanine (N terminus(CP(RK→A))) or deletion of only the section with the highest charge density (N terminusΔCP-strict) (Figure 4A) completely abolished condensate formation (Figures 4C, 4D, and S3; Video S5) and prevented, or considerably delayed, respectively, recruitment to chromosomes upon mitotic exit (Figure 4E). Consistent with this result, we found that full-length Ki-67 with charge-neutralizing mutations in the CP region (Ki-67(CP(RK→A))) or deletion of the CP section with the highest charge density (Ki-67ΔCP-strict) failed to cluster chromosomes to the same extent as wild-type Ki-67 (Figures 4F, 4G, and S2H; Video S6). We conclude that, during mitotic exit, enrichment of Ki-67 on chromosomes, Ki-67 condensate formation, and chromosome clustering rely on the high density of positive charges within the Ki-67 N terminus.

### Ki-67 phosphorylation counteracts chromosome clustering

To explore the role of phosphorylation in the function of the Ki-67 CP region, we restored the ten glutamate mutations of the phosphomimetic construct that are located in the CP region (Ki-67(129E); Figure 5A). In contrast to the original phosphomimetic Ki-67(139E) construct, the Ki-67(129E) version formed condensates upon mitotic exit (Figures 5A–5D) and supported chromosome clustering (Figures 5E, 5F, and S2I), albeit to a lesser extent than wild-type Ki-67. These findings suggest that some of the remaining phosphorylation sites, which are mostly located in the repeat sequences of Ki-67 (Figure 5A), also need to be dephosphorylated to complete chromosome clustering.

We considered that dephosphorylation of these sites might be required to collapse the Ki-67 extended structure and allow complete chromosome clustering. To test this hypothesis, we measured the extension of the protein at the chromosome surface by utilizing Ki-67 constructs tagged with mCherry and EGFP at the N and C termini, respectively. While the wild-type version decreased its distance between the fluorophores at mitotic exit to 29 nm (± 15 nm), the phosphomimetic Ki-67 mutants remained significantly more extended (85 ± 52 nm for Ki-67(139E), 58 ± 34 nm for Ki-67(129E); mean ± SD), despite similar expression levels (Figures 5G–5I and S2J). This suggests that complete Ki-67 dephosphorylation is required for collapsing its molecular structure. Phosphorylation, on the other hand, promotes its extension in early mitosis since the height of the phosphomimetic Ki-67 mutants was significantly larger. In summary, we conclude that Ki-67 phosphorylation counteracts chromosome clustering in two ways; by inhibiting its collapse and by neutralizing the positively CP.

### RNA is critical for chromosome clustering

How does the high density of positive charges mediate Ki-67 phase separation? Since RNA has been suggested as a universal factor that regulates phase separation[12,23,24] and RNAs localize to the chromosome surface,[7,25] we co-imaged newly synthesized RNA and Ki-67 in cells undergoing mitosis. Using a double thymidine release strategy, we labeled newly synthesized RNAs by an 5-ethynyluridine (EU) pulse for 3 h before cells entered mitosis and assessed RNA localization in cells undergoing metaphase and anaphase.

The localization pattern of Ki-67 and newly synthesized RNA largely overlapped on the mitotic chromosome surface and in the cytoplasmic Ki-67 condensates that formed during anaphase (Figure 6A). By contrast, in Ki-67 KO cells, RNA binding to chromosomes during metaphase and its increase during anaphase were strongly reduced (Figure 6B), resulting in RNA accumulation in large cytoplasmic foci (Figure 6A). This suggests that Ki-67 recruits RNAs to the chromosome surface during early mitosis and mitotic exit.

To test whether RNA is crucial for Ki-67 condensate formation, we acutely depleted RNA in mitotically arrested cells by microinjecting RNase A (Figures 6C–6E). Remarkably, after induction of mitotic exit, RNase A-injected cells consistently failed to form cytoplasmic foci, unlike dextran-injected or non-injected cells. By contrast, Ki-67 enrichment on chromosomes was not affected by acute RNA removal. Unfortunately, we could not address the effect of acute RNA removal on chromosome clustering since microinjection of spindle-less cells was impossible, likely due to their lack of mechanical resistance and because microinjection itself affected chromosome morphology (as seen with dextran injection). Nevertheless, this experiment highlights that RNA is necessary for Ki-67 condensate formation during mitotic exit.

**Figure 3. A positively CP in the Ki-67 N terminus drives phase separation, early-anaphase chromosomal enrichment, and clustering**

(A) Design of Ki-67 constructs. Disorder (blue high, red low), charge (blue positive, red negative, sliding window 100), and low-complexity prediction (blue, sliding window size 45). CP, charged patch (186 aa); FASI, fragment absent in short isoform (360 aa); LR, leucine/arginine-rich DNA-binding domain.

(B) EGFP-labeled Ki-67 domains transfected into Ki-67 KO cells imaged during spindle-less mitotic exit. White lines indicate chromosomal regions used in (C).

(C) EGFP total fluorescence intensity in chromosomal regions over time as in (B) ($n \geq 23$).

(D) Quantification of cytoplasmic condensates over time as in (B) ($n \geq 23$).

(E) Time-lapse of Ki-67 KO cells expressing EGFP-labeled full-length Ki-67 or constructs with domain deletions undergoing spindle-less mitotic exit. DNA labeled with SiR-Hoechst.

(F) Chromosome ensemble area over time as in (E) ($n \geq 19$).

Dashed lines indicate flavopiridol addition (C, D, and F). Lines/shaded areas represent mean ± SD (C and F) or mean ± SEM (D). Max. intensity z-projections shown. Scale bars, 10 μm.

CellPress
OPEN ACCESS

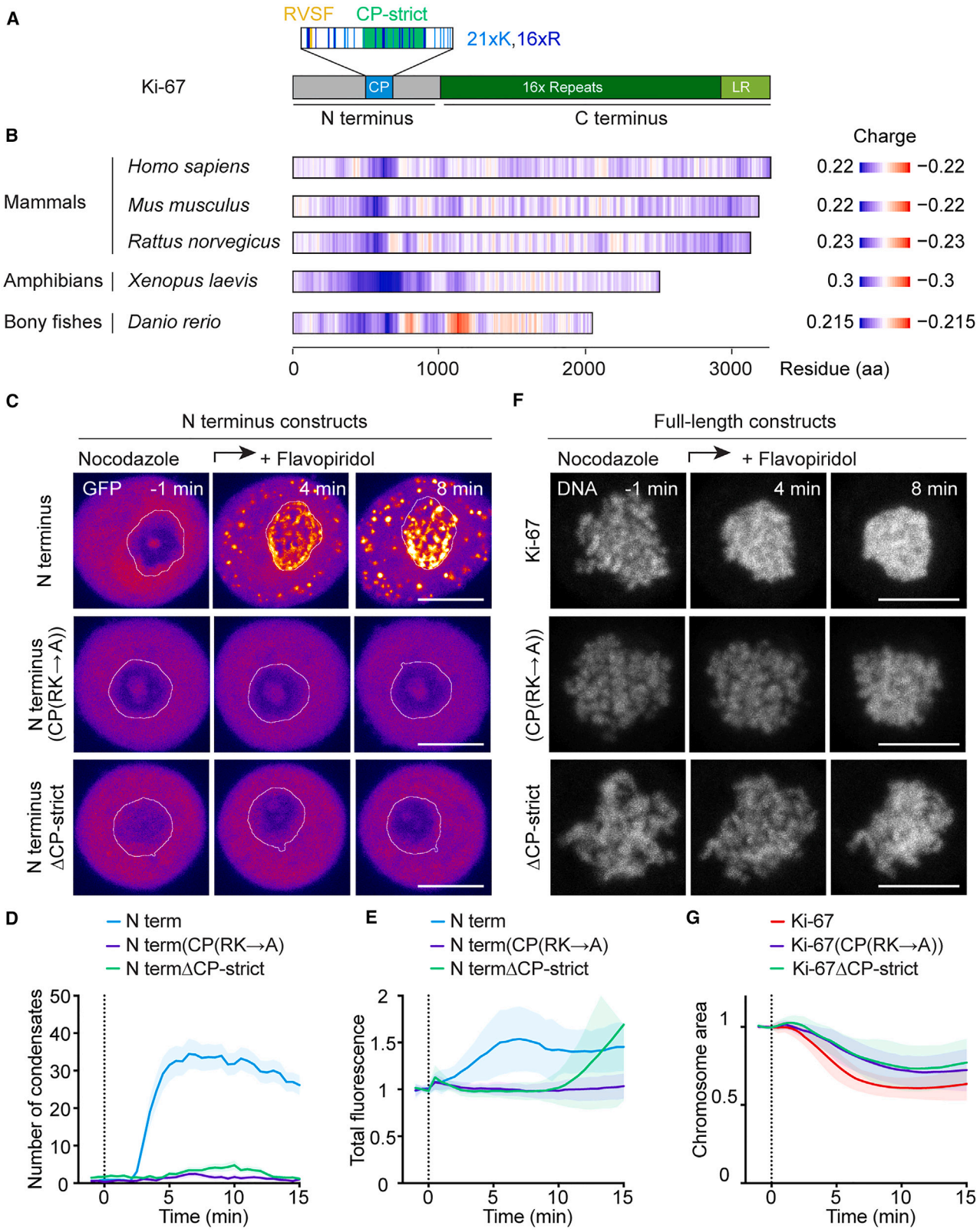


(legend on next page)

To determine which types of RNAs might be relevant for Ki-67 condensate formation, we visualized mRNAs (Figures S5A and S5B) and ribosomal RNAs (rRNAs) (Figures S5C and S5D) in endogenously tagged EGFP-Ki-67 cells using FISH probes. While mRNAs localized to the cytoplasm, premature rRNAs were enriched on the surface of anaphase chromosomes consistent with a previous report[7,26] and co-localized with Ki-67 in cytoplasmic foci.

Based on the co-condensation of Ki-67 and premature rRNA, we aimed to test whether premature rRNAs might be important for Ki-67 condensate formation and chromosome clustering. We used endogenously tagged Ki-67 cells and selectively inhibited RNA polymerase I, the enzyme responsible for transcribing rRNA, for 2–5 h before cells entered mitosis using low doses of actinomycin D (Act D). As expected, the addition of Act D decreased premature rRNA levels on chromosomes (Figures S5C and S5D). Interestingly, Act D treatment neither affected chromosome dispersal upon mitotic entry nor Ki-67 enrichment during mitotic exit (Figures 6F, 6G, and 6I). However, it considerably reduced Ki-67 condensate formation (Figure 6H) and chromosome clustering (Figures 6I and 6J; Video S7). To ensure these effects are not due to side-effects of Act D, we confirmed these results with a different RNA polymerase I inhibitor, BMH-21, and obtained consistent results in an endogenously mCherry-tagged Ki-67 cell line (Figures S6A–S6D) as well as in wild-type cells (Figures S6E–S6G). By contrast, inhibition of RNA polymerase II, the enzyme transcribing protein-coding genes, by alpha-amanitin did not affect condensate formation or chromosome clustering (Figures 6F–6J), supporting the role of premature rRNAs in Ki-67 condensate formation and chromosome clustering.

The observation that premature rRNA depletion impairs chromosome clustering despite normal Ki-67 enrichment on chromosomes implies that chromosome clustering is not mediated by chromosome bridging through the formation of a second DNA-binding site within Ki-67. Thus, it is tempting to speculate that RNA-mediated condensation of Ki-67 is key to chromosome clustering.

## Co-condensation of Ki-67 and RNA leads to chromosome clustering in coarse-grained simulations

To gain insight into the molecular mechanism leading to RNA-mediated chromosome clustering, we performed molecular dynamics simulations using a minimal coarse-grained model (see STAR Methods). In these simulations, Ki-67 and RNA were modeled as chains of charged beads connected by springs. Ki-67 is represented as 24 beads, with the charges of each bead "calculated" based on the underlying amino acids with or without 150 phosphorylated residues (Table S1; Figure 7A). To model Ki-67 dephosphorylation during mitotic exit, we assigned a charge that corresponds to 150 phosphorylation sites to each Ki-67 molecule and increased the charge as the simulation progressed until the molecule reached the net charge of fully dephosphorylated Ki-67 (Figures 7A and 7B). The charge variation followed a smooth sigmoidal function to mimic the gradual removal of phosphate groups by phosphatases in cells. Ions and phosphate groups were not modeled explicitly, but the effect of the solvent was taken into account indirectly by a screening term added to the electrostatic potential acting between the beads. The grafting density and brush height of Ki-67 were modeled to match measurements observed in cells.[8]

To characterize the forces acting between two chromosome surfaces, we modeled chromosomes as immobile surfaces decorated with grafted Ki-67 molecules and added freely diffusing RNA molecules (Figures S7A and S7B). When Ki-67 was in its phosphorylated state, the pressure acting on the two surfaces (force per unit area) was positive, indicating a repulsive force between the surfaces. As Ki-67 became increasingly dephosphorylated, the pressure between chromosome surfaces decreased until it reached a negative equilibrium value, indicating an attractive force (Figure S7B). In this state, the attractive force was generated by negatively charged RNA molecules that interacted primarily with the positively CPs of Ki-67 molecules, forming Ki-67/RNA "bridges" between the two chromosome surfaces.

Consistent with the notion that RNA and Ki-67 are necessary for the generation of attractive forces between chromosomes, we observed near-zero pressure (i.e., no attraction) between chromosomes in simulations performed in the absence of either RNA or Ki-67 (Figures S7A and S6B). Our simulations thus show that negatively charged RNA does not simply adsorb onto the positively charged (dephosphorylated) Ki-67 brushes, neutralizing their charge. Instead, it generates an attractive force between the chromosomes. Additionally, the simulations show that Ki-67/RNA bridges are more frequent in the presence of the CP, and that removing the latter leads to the formation of much fewer Ki-67/RNA bridges and thus to a measurable decrease in the inter-chromosome attraction (Figures S7A and S7B).

To explore the dynamics of chromosome clustering driven by Ki-67/RNA interactions, we modeled chromosomes as mobile half-cylinders grafted with Ki-67 molecules in an environment

**Figure 4. High positive-charge density in Ki-67 N terminus is conserved and essential for chromosome clustering**

(A) Schematic of Ki-67's N-terminal segment. CP, charged patch (186 aa) with lysine (K) and arginine (R) residues. RVSF, protein phosphatase binding motif mutated to RASA in Figure S4. CP-strict, charge patch-strict (77 aa).

(B) Charge heatmaps of predicted Ki-67 orthologues (charge: blue positive, red negative, sliding window 100).

(C) Time-lapse of spindle-less mitotic exit of Ki-67 KO cell expressing different Ki-67 N terminus constructs tagged with EGFP. White lines represent chromosomal regions used in (E).

(D) Quantification of cytoplasmic condensates over time as in (C) ($n \geq 19$).

(E) EGFP total fluorescence intensity in segmented chromosome ensemble area over time as in (C) ($n \geq 19$).

(F) Time-lapse of spindle-less mitotic exit of Ki-67 KO cell expressing indicated constructs. DNA labeled with SiR-Hoechst.

(G) Chromosome ensemble area over time as in (F) ($n \geq 25$).

Dashed lines indicate flavopiridol addition (D, E, and G). Lines/shaded areas represent mean ± SEM (D) or mean ± SD (E and G). Max. intensity z-projections shown. Scale bars: 10 μm in (C) and (F).

CellPress
OPEN ACCESS

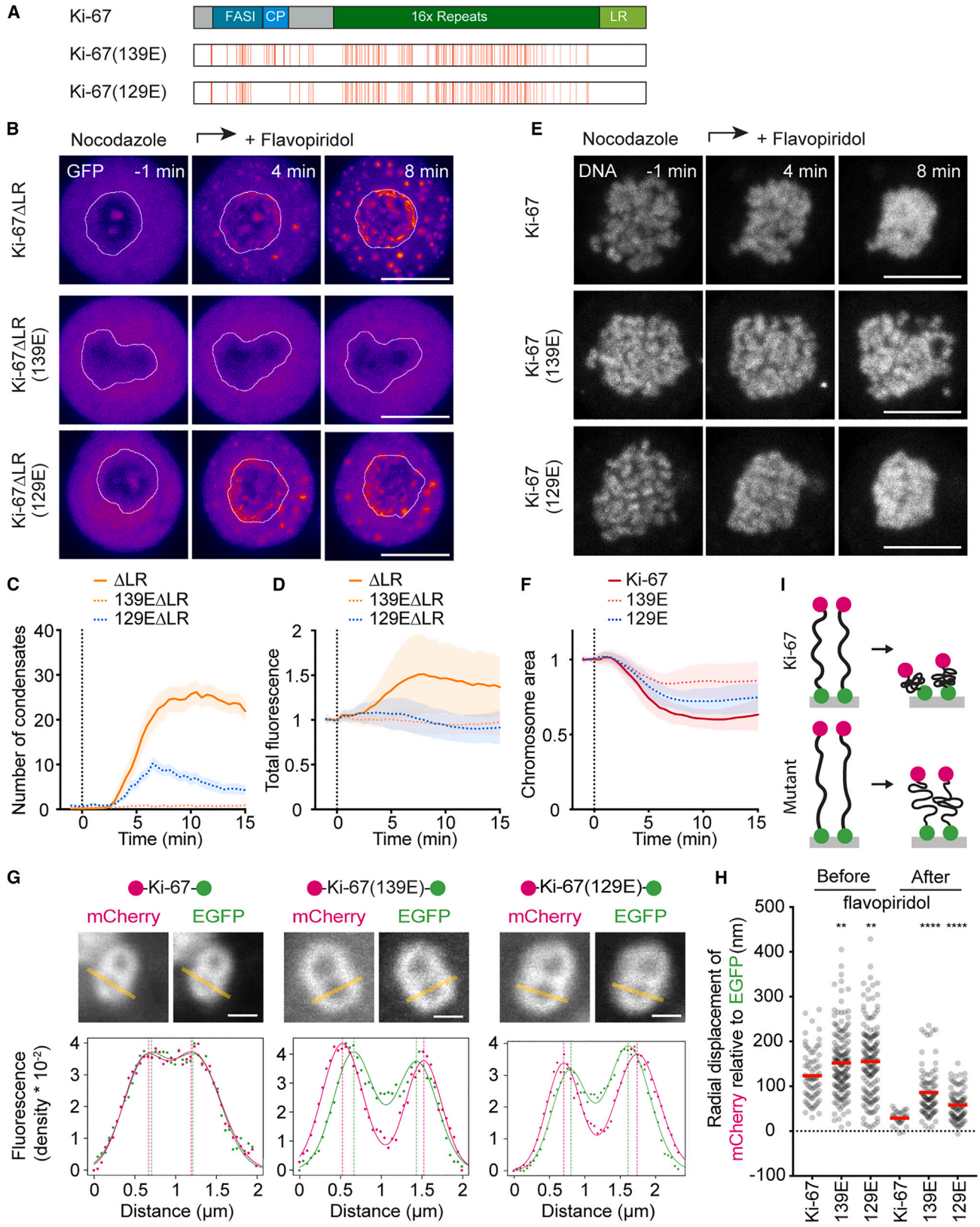


(legend on next page)

of freely diffusing Ki-67 and RNA molecules (Figure 7C). Consistent with our experimental data (Figures 1A, 2, and 6A), the distance between the two chromosomes in the simulations decreased with increasing dephosphorylation of Ki-67, until an equilibrium distance was reached at which the two chromosomes were separated by a dense layer of Ki-67 mixed with RNA (Figures 7C and 7D; Video S8). In addition, in the simulations, free Ki-67 molecules formed condensates with RNA independently of the presence of chromosomes (Figures 7C and 7E). Both condensate formation and chromosome clustering depended on the presence of RNA (Figures 7C and 7D; Video S9), indicating that co-condensation between Ki-67 and RNA would be sufficient to bring chromosomes together. Overall, our coarse-grained simulations (1) validate the proposed physical mechanism, (2) qualitatively reproduce the results of our cell-based experiments, and (3) highlight the importance of RNA in chromosome clustering.

## DISCUSSION

Our experiments and simulations support a model (Figure 7F) in which, during early mitosis, phosphorylated Ki-67 extends from the chromosome surface, dispersing chromosomes by a surfactant-like mechanism.[8] Upon mitotic exit, Ki-67 dephosphorylation causes the collapse of its extended structure and exposes a conserved positively CP within its amino terminus. This change in properties reduces Ki-67's amphiphilicity at the chromosome-cytoplasm interface and, concomitant with RNA recruitment, trigger Ki-67's transition from a repulsive to a condensed state. We propose that Ki-67 condensation with RNA at the surface of chromosomes promotes chromosome clustering and, together with the concerted collapse of Ki-67, drives the exclusion of cytoplasmic material (Figures S7C–S7F) before nuclear envelope reformation (Cuylen-Haering et al.[11]; Figures S1K and S1L).

A recent publication reported that single or multiple Ki-67 repeats can undergo phase separation *in vitro*, which is enhanced by phosphorylation.[13] This finding, in combination with the dynamic turnover of Ki-67 on chromosomes measured by FRAP and its dissociation from chromosomes observed upon sodium acetate treatment, led to the suggestion that Ki-67 might form a liquid-like phase on the surface of chromosomes during early mitosis. However, how such a liquid layer could contribute to chromosome dispersion during early mitosis was not addressed.

We suggest that the opposite is the case: when two surfaces coated with a liquid interact, coalescence of the liquid layers should generate forces that bring the respective surfaces together—a feature that is in line with chromosome clustering rather than with chromosome dispersion. Our data suggest that Ki-67 forms a liquid-like coat around chromosomes exclusively during exit from mitosis, triggered by its dephosphorylation (Figures 1 and 2) and RNA interaction (Figure 6). This process, in turn, promotes chromosome clustering, which effectively excludes cytoplasmic material (Figures S7C–S7F). During early mitosis, phosphorylation of Ki-67 instead inhibits condensate formation (Figure 2) and causes the molecule to extend perpendicularly on the chromosome surface (Figures 5G–5I). Considering that phosphorylated Ki-67 likely has a negative net charge (Table S1), the extension away from the chromatin surface might be the result of the repulsion between negative charges of both phosphorylated Ki-67 and chromatin. This leads to the formation of an electrostatic and steric barrier consistent with a surfactant-like mechanism.

The difference between our cellular findings and these earlier *in vitro* data,[13] especially regarding the specific region of Ki-67 responsible for phase separation and the impact of phosphorylation, may be attributed to the lack of RNA in the *in vitro* assays as well as to the use of high concentrations of both protein (40 μM in most *in vitro* assays as opposed to 50 nM endogenous in the cytoplasm [Figure S1H]) and crowding agents.

On the other hand, our findings support the notion that Ki-67's interaction with RNA is key to phase separation and chromosome clustering. Several studies suggested that Ki-67 interacts either directly or indirectly with RNA: Ki-67 depletion caused loss of newly synthesized RNAs from chromosomes in early mitosis,[7] recombinantly expressed Ki-67 fragments such as the fork-head associated (FHA) domain or three tandem repeats, and pulled down premature rRNAs from total RNA;[26] the nucleolar protein interacting with the FHA domain of Ki-67 (NIFK) is a putative RNA-binding protein.[27] Since NIFK binding depends on mitotic phosphorylation, it likely does not contribute to RNA

**Figure 5. Complete Ki-67 dephosphorylation is required for full chromosome clustering**

(A) Position of 139 serine or threonine to glutamate (E) substitutions to generate phosphomimetic Ki-67(139E) marked by red lines. In Ki-67(129E), 10 substitutions in the charged patch (CP) are reverted to wild-type.

(B) Time-lapse of Ki-67 KO cells expressing EGFP-labeled Ki-67ΔLR constructs undergoing spindle-less mitotic exit.

(C) Quantification of cytoplasmic condensates over time as in (B). Ki-67ΔLR and Ki-67(139E)ΔLR shown for reference as in Figure 2G; $n = 31$ (Ki-67(129E)ΔLR).

(D) EGFP total fluorescence intensity in chromosome ensemble area over time as in (B). Ki-67ΔLR and Ki-67(139E)ΔLR shown for reference as in Figure 2H; $n = 31$ (Ki-67(129E)ΔLR).

(E) Time-lapse of Ki-67 KO cells expressing full-length EGFP-labeled Ki-67 constructs during spindle-less mitotic exit. DNA labeled with SiR-Hoechst.

(F) Chromosome ensemble area over time as in (E). Ki-67 and Ki-67(139E) shown for reference as in Figure 2E; $n = 22$ (Ki-67(129E)).

(G) Indicated Ki-67 constructs with mCherry at the N terminus and EGFP at the C terminus on mitotic chromosomes (taxol arrest) before and after flavopiridol addition (top). Images (middle) depict sister chromatid pairs oriented perpendicular to the imaging plane after flavopiridol addition. Yellow lines indicate measurements for mCherry and EGFP (bottom). Sum of two Gaussian functions (lines) fit to the fluorescence densities (dots) along line profiles of each channel to determine peak positions (dashed lines).

(H) Relative molecular extensions calculated from mCherry and EGFP radial displacements (mCherry peak-to-peak distance—EGFP peak-to-peak distance/2) from line profile measurements as in (G). $n \geq 72$ (before flavopiridol), $n \geq 29$ (after flavopiridol).

(I) Model of Ki-67's molecular organization on chromosomes during early mitosis and during mitotic exit.

Dashed lines indicate flavopiridol addition (C, D, and F). Lines/shaded areas represent mean ± SEM (C) or mean ± SD (D and F). Red bars indicate mean (H); significance was tested versus Ki-67 by two-tailed unpaired t test (Before flavopiridol, 139E, ** $p = 3.2 \times 10^{-3}$; 129E, ** $p = 3.4 \times 10^{-3}$; after flavopiridol, 139E, **** $p = 4.7 \times 10^{-8}$; 129E, **** $p = 1.6 \times 10^{-5}$). Max. intensity z-projections (B and E) or single z-slices (G) shown. Scale bars: 10 μm in (B) and (E) or 1 μm in (G).

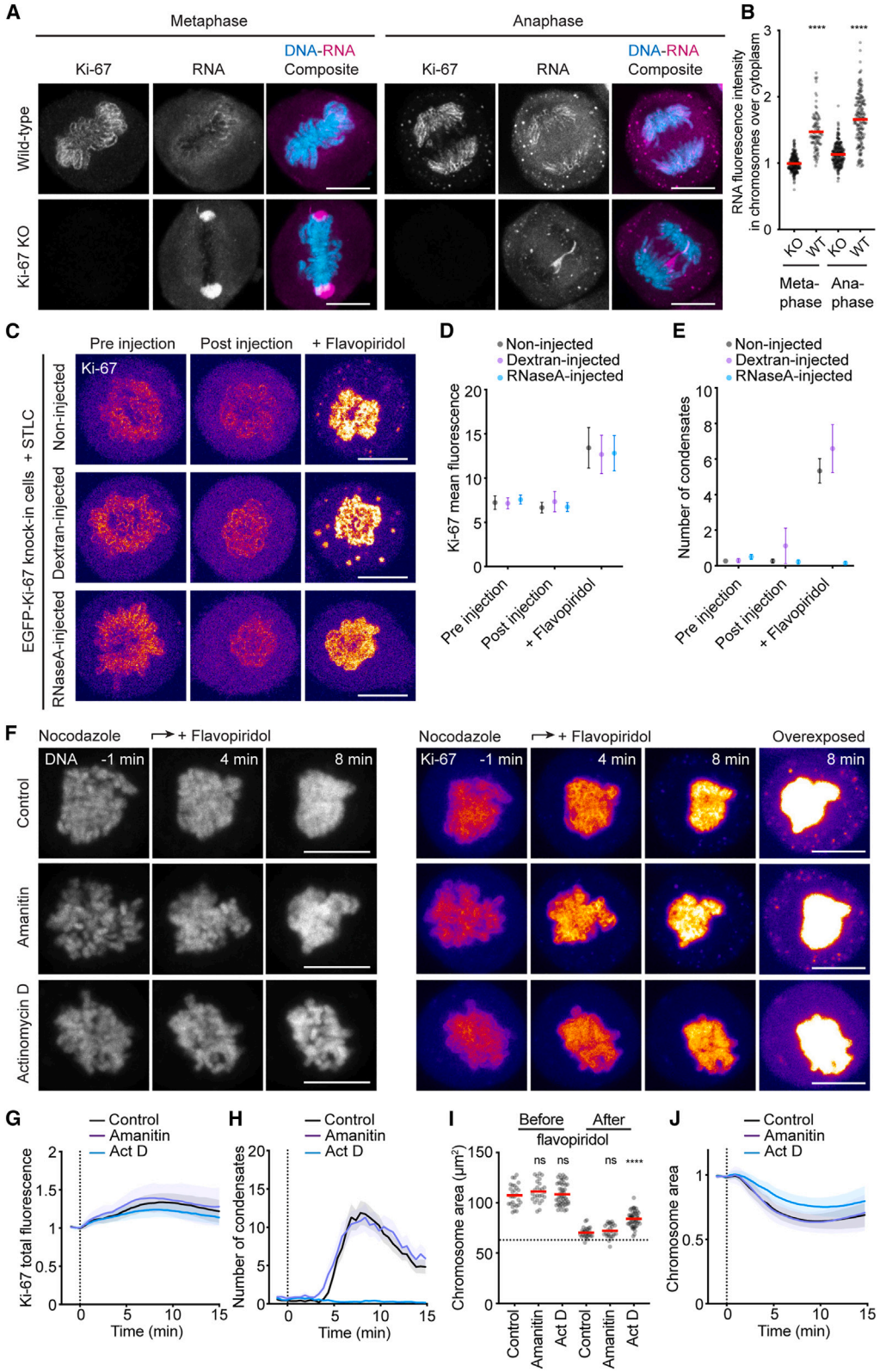


*(legend on next page)*

recruitment during mitotic exit. Nevertheless, indirect RNA enrichment on chromosomes through other proteins recruited by Ki-67 during mitosis[4,28,29] remains a possibility. Yet, based on the results of our experiments and simulations, it is tempting to speculate that direct complementary electrostatic interactions between negatively charged RNA molecules and Ki-67's positively CP contribute to their co-condensation.[30,31]

The selective impairment of chromosome clustering upon removal of premature rRNAs, as opposed to polyadenylated mRNAs (Figures 6F–6J), raises questions about the origin of this specificity. Considering that approximately 80% of RNAs in human cells are rRNAs, sheer abundance might play a role. Alternatively, initial rRNA transcripts are significantly longer than the average mRNA transcript, suggesting that RNA length could be a critical factor. However, to validate the detailed molecular mechanism and understand the RNA specificity in Ki-67-mediated chromosome clustering, *in vitro* studies with full-length Ki-67 will ultimately be necessary.

Other recent studies have shown that natural or artificial DNA-bound condensates can generate forces that remodel chromatin *in vitro*[32–34] or in cells[35] to mediate compaction or exclusion of chromatin. Our data suggest that electrostatic interactions contribute to the generation of a condensed phase on the surface of mitotic chromosomes, generating large enough adhesive forces to facilitate their clustering. The force-generating interface of the Ki-67/RNA condensed phase could in physical terms be viewed as capillary forces, which are well-known in non-living soft matter systems[36] and have been suggested to play a role in multicellular tissue organization[37,38] and intracellular condensate remodeling.[39] However, distinguishing between surface-mediated co-condensation forces and charge-driven bridging interactions remains an important and highly challenging problem in multicomponent systems, particularly in cellular contexts. Regulated protein surfactants[8,40,41] and surface-adsorbed condensates[42] might have implications at surfaces and interfaces of other membrane-less biomolecular condensates for generating mechanical forces and structuring biomolecular condensates.

Previous studies based on Ki-67 KO cells have suggested that Ki-67 may not be necessary for cell viability[43,44] and consequently for maintaining chromosome stability. However, without Ki-67, chromosomes remain coalesced throughout mitosis. This raises the question: How important is chromosome clustering during mitotic exit if chromosomes are dispersed in early mitosis? Persistent chromosome dispersal, as observed in chromosome clustering-deficient Ki-67 mutants, might pose greater challenges than continual chromosome coalescence. It will be interesting to test the effect of clustering-deficient Ki-67 mutants on chromosome stability and cell viability, particularly in model systems where chromosomes are notably spaced apart such as embryos.

## Limitations of the study

First, our experiments using phosphomimetic mutants suggest that dephosphorylation is key for Ki-67 phase separation and chromosome clustering. However, due to potential differences between glutamates/aspartates and phosphorylated serines/threonines, future *in vitro* studies will be necessary to directly test the role of phosphorylation in Ki-67's functions. Second, while the CP is required for Ki-67 phase separation, we lack direct experimental evidence that Ki-67 binds RNA via the CP, and it remains uncertain if Ki-67 specifically binds premature rRNA. We cannot rule out that other RNAs species bind to chromosomes and contribute to condensate formation and clustering. Additionally, secondary effects of premature rRNA depletion during the Act D or BMH-21 treatment could affect chromosome clustering in unknown ways. Finally, our computational model is near-minimal to test the general possible physical mechanism at play. It lacks molecular details and chemical specificity, such as the molecular details of Ki-67, RNA and chromatin, ions and counterions, solvation, and additional nucleolar components that might participate in the process. Some of these elements could be included in a more detailed, coarse-grained, or atomistic model to explore possible chemical specificity of the process.

## STAR★METHODS

Detailed methods are provided in the online version of this paper and include the following:

**Figure 6. RNA is critical for chromosome clustering**

(A) Immunofluorescence images of wild-type (WT) and Ki-67 KO cells (KO) co-seeded to reduce staining variability. Newly synthesized RNAs labeled by an EU pulse for 3 h before mitosis.

(B) Mean fluorescence intensity of EU-labeled RNA in DAPI-labeled chromosomes divided by cytoplasmic mean fluorescence intensity as in (A), normalized to Ki-67 KO cells in metaphase. Individual chromosome sets are plotted ($n \geq 109$). Significance was tested by two-tailed unpaired t test (metaphase, KO & WT, **** $p = 1 \times 10^{-15}$; anaphase, KO & WT, **** $p = 1 \times 10^{-15}$).

(C) RNase A injection in live EGFP-Ki-67 knockin cells arrested in prometaphase by STLC. Flavopiridol added 10–15 min after injection, imaged again 7–11 min after addition (+ flavopiridol).

(D) EGFP mean fluorescence intensity in segmented chromosome area as in (C) ($n \geq 14$).

(E) Quantification of EGFP-Ki-67 cytoplasmic condensates as in (C) ($n \geq 14$).

(F) Time-lapse of EGFP-Ki-67 knockin cells undergoing spindle-less mitotic exit, untreated or with indicated treatments for 2–5 h before mitosis. DNA labeled with SiR-Hoechst.

(G) EGFP total fluorescence intensity in segmented chromosome area over time as in (F).

(H) Quantification of EGFP-Ki-67 cytoplasmic condensates over time as in (F).

(I) Chromosome ensemble area before and 8 min after flavopiridol addition of EGFP-Ki-67 knockin cells as in (F), plotted in (J). Dashed line indicates mean chromosome ensemble area of Ki-67 KO cells from Figure 1E for reference. Significance was tested by unpaired t test relative to control conditions (before flavopiridol, amanitin, ns $p = 0.19$, Act D, ns $p = 0.66$; after flavopiridol, amanitin, ns $p = 0.28$, Act D, **** $p = 2.1 \times 10^{-12}$).

(J) Chromosome ensemble area over time as in (F).

Dashed lines indicate flavopiridol addition (G, H, and J). Red bars indicate mean (B and I). Dots and bars represent mean ± SD (D) or mean ± SEM (E). Lines/shaded areas represent mean ± SD (G and J) or mean ± SEM (H). Max. intensity z-projections shown. $n \geq 26$ (G–J). Scale bars: 10 μm in (A), (C), and (F).

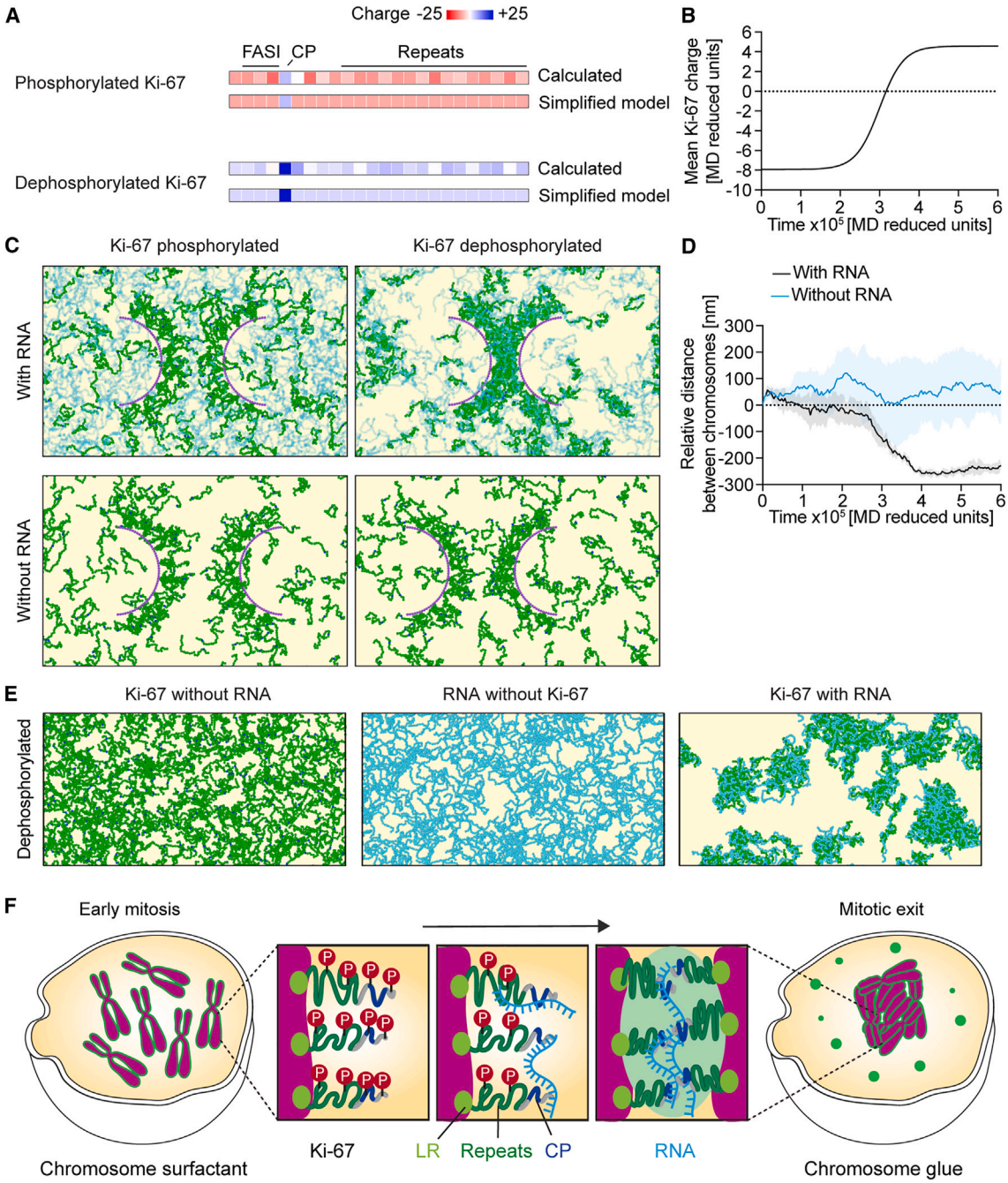


**Figure 7. RNA is required for chromosome clustering in coarse-grained simulations**

(A) Ki-67 bead model. Ki-67 is depicted as a chain of 24 beads, color coded by calculated charge based on amino acid contents (calculated; see Table S1). The phosphorylated form considers 150 phosphorylation sites. In the simulation (simplified model), the charged patch (CP) retains the calculated charge, while the other beads are assigned an average charge.

(B) Variation of mean Ki-67 charge per bead over simulation time, mimicking the switch from 150 phosphosites to fully dephosphorylated Ki-67.

(C and D) Simulation of chromosome clustering as Ki-67 charge is gradually increased as in (B). Chromosomes are modeled as half-cylinders (violet) decorated with bead-spring polymers representing Ki-67 molecules (green—CP in dark blue). RNA molecules (light blue) shown as semi-transparent.

(C) Snapshots (top view) corresponding to early mitosis (left) or mitotic exit (right).

(D) Relative distance (subtracting initial distance) between the centers of mass of the two chromosomes over simulation time using the gradual Ki-67 charge increase as in (B). $n = 5$.

(E) Simulations of Ki-67 and RNA condensation in solution as the charge of Ki-67 is gradually increased as in (B). Snapshots of dephosphorylated Ki-67 (green—CP in dark blue) with or without RNA (light blue) and RNA without Ki-67.

*(legend continued on next page)*

## SUPPLEMENTAL INFORMATION

Supplemental information can be found online at https://doi.org/10.1016/j.molcel.2024.07.022.

## ACKNOWLEDGMENTS

We thank Daniel W. Gerlich for providing cell lines, the EMBL Advanced Light Microscopy Facility (ALMF) for support, Christian H. Haering and Thomas Quail for input on the manuscript, and Martina Dees for cloning several Ki-67 constructs. This work was supported by the German Research Foundation (DFG project number 402723784) and the Human Frontier Science Program (CDA00045/2019). A.H.-A. and A.B. have received PhD fellowships from the Boehringer Ingelheim Fonds, V.S. and A.Ś. were supported by the European Research Council (ERC) under the European Union's Horizon 2020 research and innovation programme (grant no. 802960), and Y.H. was supported by a fellowship from the EMBL interdisciplinary Postdoc (EIPOD) program (Marie Sklodowska-Curie Actions, COFUND grant agreement 664726).

## AUTHOR CONTRIBUTIONS

A.H.-A. and S.C.-H. conceived the project. A.H.-A. designed, performed, and analyzed all experiments except those mentioned next. Y.H. performed microinjection experiments, performed experiments with Ki-67(139DΔLR), and contributed to RNA experiments. Z.K. performed oligo(dT) FISH experiments. A.B. helped A.H.-A. with the acquisition of FCS-calibrated imaging. V.S. and A.Ś. designed simulations. V.S. performed and analyzed simulations. S.C.-H. acquired funding and supervised the project. S.C.-H., A.H.-A., A.Ś., and V.S. wrote the manuscript with feedback from J.E.

## DECLARATION OF INTERESTS

The authors declare no competing interests.

Received: October 26, 2023
Revised: June 4, 2024
Accepted: July 24, 2024
Published: August 16, 2024

## REFERENCES

1. Paulson, J.R., Hudson, D.F., Cisneros-Soberanis, F., and Earnshaw, W.C. (2021). Mitotic chromosomes. Semin. Cell Dev. Biol. *117*, 7–29. https://doi.org/10.1016/j.semcdb.2021.03.014.
2. van der Zanden, S.Y., Jongsma, M.L.M., Neefjes, A.C.M., Berlin, I., and Neefjes, J. (2023). Maintaining soluble protein homeostasis between nuclear and cytoplasmic compartments across mitosis. Trends Cell Biol. *33*, 18–29. https://doi.org/10.1016/j.tcb.2022.06.002.
3. Booth, D.G., and Earnshaw, W.C. (2017). Ki-67 and the Chromosome Periphery Compartment in Mitosis. Trends Cell Biol. *27*, 906–916. https://doi.org/10.1016/j.tcb.2017.08.001.
4. Stenström, L., Mahdessian, D., Gnann, C., Cesnik, A.J., Ouyang, W., Leonetti, M.D., Uhlén, M., Cuylen-Haering, S., Thul, P.J., and Lundberg, E. (2020). Mapping the nucleolar proteome reveals a spatiotemporal organization related to intrinsic protein disorder. Mol. Syst. Biol. *16*, e9469. https://doi.org/10.15252/msb.20209469.
5. le Hernandez-Verdun, D., and Gautier, T. (1994). The chromosome periphery during mitosis. BioEssays *16*, 179–185. https://doi.org/10.1002/bies.950160308.
6. Booth, D.G., Takagi, M., Sanchez-Pulido, L., Petfalski, E., Vargiu, G., Samejima, K., Imamoto, N., Ponting, C.P., Tollervey, D., Earnshaw, W.C., and Vagnarelli, P. (2014). Ki-67 is a PP1-interacting protein that organises the mitotic chromosome periphery. eLife *3*, e01641. https://doi.org/10.7554/eLife.01641.
7. Hayashi, Y., Kato, K., and Kimura, K. (2017). The hierarchical structure of the perichromosomal layer comprises Ki67, ribosomal RNAs, and nucleolar proteins. Biochem. Biophys. Res. Commun. *493*, 1043–1049. https://doi.org/10.1016/j.bbrc.2017.09.092.
8. Cuylen, S., Blaukopf, C., Politi, A.Z., Müller-Reichert, T., Neumann, B., Poser, I., Ellenberg, J., Hyman, A.A., and Gerlich, D.W. (2016). Ki-67 acts as a biological surfactant to disperse mitotic chromosomes. Nature *535*, 308–312. https://doi.org/10.1038/nature18610.
9. Verheijen, R., Kuijpers, H.J., van Driel, R., Beck, J.L., van Dierendonck, J.H., Brakenhoff, G.J., and Ramaekers, F.C. (1989). Ki-67 detects a nuclear matrix-associated proliferation-related antigen. II. Localization in mitotic cells and association with chromosomes. J. Cell Sci. *92*, 531–540. https://doi.org/10.1242/jcs.92.4.531.
10. Uhlmann, F., Lottspeich, F., and Nasmyth, K. (1999). Sister-chromatid separation at anaphase onset is promoted by cleavage of the cohesin subunit Scc1. Nature *400*, 37–42. https://doi.org/10.1038/21831.
11. Cuylen-Haering, S., Petrovic, M., Hernandez-Armendariz, A., Schneider, M.W.G., Samwer, M., Blaukopf, C., Holt, L.J., and Gerlich, D.W. (2020). Chromosome clustering by Ki-67 excludes cytoplasm during nuclear assembly. Nature *587*, 285–290. https://doi.org/10.1038/s41586-020-2672-3.
12. Banani, S.F., Lee, H.O., Hyman, A.A., and Rosen, M.K. (2017). Biomolecular condensates: organizers of cellular biochemistry. Nat. Rev. Mol. Cell Biol. *18*, 285–298. https://doi.org/10.1038/nrm.2017.7.

(F) Working model: during early mitosis, Ki-67 is heavily phosphorylated and extended, allowing chromosome dispersal. During mitotic exit, gradual dephosphorylation occurs, causing Ki-67 to phase separate with RNA and the collapse of Ki-67, promoting coalescence of neighboring chromosome surfaces and clustering of chromosomes.
Dashed lines (B and D) are drawn at y = 0 for reference. Lines/shaded areas represent mean ± SD (D).

13. Yamazaki, H., Takagi, M., Kosako, H., Hirano, T., and Yoshimura, S.H. (2022). Cell cycle-specific phase separation regulated by protein charge blockiness. Nat. Cell Biol. *24*, 625–632. https://doi.org/10.1038/s41556-022-00903-1.

14. Endl, E., and Gerdes, J. (2000). Posttranslational modifications of the Ki-67 protein coincide with two major checkpoints during mitosis. J. Cell. Physiol. *182*, 371–380. https://doi.org/10.1002/(SICI)1097-4652(200003)182:3<371::AID-JCP8>3.0.CO;2-J.

15. Potapova, T.A., Daum, J.R., Pittman, B.D., Hudson, J.R., Jones, T.N., Satinover, D.L., Stukenberg, P.T., and Gorbsky, G.J. (2006). The reversibility of mitotic exit in vertebrate cells. Nature *440*, 954–958. https://doi.org/10.1038/nature04652.

16. Takagi, M., Matsuoka, Y., Kurihara, T., and Yoneda, Y. (1999). Chmadrin: a novel Ki-67 antigen-related perichromosomal protein possibly implicated in higher order chromatin structure. J. Cell Sci. *112*, 2463–2472. https://doi.org/10.1242/jcs.112.15.2463.

17. Samwer, M., Schneider, M.W.G., Hoefler, R., Schmalhorst, P.S., Jude, J.G., Zuber, J., and Gerlich, D.W. (2017). DNA Cross-Bridging Shapes a Single Nucleus from a Set of Mitotic Chromosomes. Cell *170*, 956–972.e23. https://doi.org/10.1016/j.cell.2017.07.038.

18. Saiwaki, T., Kotera, I., Sasaki, M., Takagi, M., and Yoneda, Y. (2005). In vivo dynamics and kinetics of pKi-67: Transition from a mobile to an immobile form at the onset of anaphase. Exp. Cell Res. *308*, 123–134. https://doi.org/10.1016/j.yexcr.2005.04.010.

19. Dephoure, N., Zhou, C., Villén, J., Beausoleil, S.A., Bakalarski, C.E., Elledge, S.J., and Gygi, S.P. (2008). A quantitative atlas of mitotic phosphorylation. Proc. Natl. Acad. Sci. USA *105*, 10762–10767. https://doi.org/10.1073/pnas.0805139105.

20. Takagi, M., Nishiyama, Y., Taguchi, A., and Imamoto, N. (2014). Ki67 Antigen Contributes to the Timely Accumulation of Protein Phosphatase 1γ on Anaphase Chromosomes. J. Biol. Chem. *289*, 22877–22887. https://doi.org/10.1074/jbc.M114.556647.

21. Wootton, J.C. (1994). Non-globular domains in protein sequences: automated segmentation using complexity measures. Comput. Chem. *18*, 269–285. https://doi.org/10.1016/0097-8485(94)85023-2.

22. Schlüter, C., Duchrow, M., Wohlenberg, C., Becker, M.H., Key, G., Flad, H.D., and Gerdes, J. (1993). The cell proliferation-associated antigen of antibody Ki-67: a very large, ubiquitous nuclear protein with numerous repeated elements, representing a new kind of cell cycle-maintaining proteins. J. Cell Biol. *123*, 513–522. https://doi.org/10.1083/jcb.123.3.513.

23. Roden, C., and Gladfelter, A.S. (2021). RNA contributions to the form and function of biomolecular condensates. Nat. Rev. Mol. Cell Biol. *22*, 183–195. https://doi.org/10.1038/s41580-020-0264-6.

24. Cochard, A., Garcia-Jove Navarro, M.G.-J., Piroska, L., Kashida, S., Kress, M., Weil, D., and Gueroui, Z. (2022). RNA at the surface of phase-separated condensates impacts their size and number. Biophys. J. *121*, 1675–1690. https://doi.org/10.1016/j.bpj.2022.03.032.

25. Gautier, T., Robert-Nicoud, M., Guilly, M.N., and Hernandez-Verdun, D. (1992). Relocation of nucleolar proteins around chromosomes at mitosis. A study by confocal laser scanning microscopy. J. Cell Sci. *102*, 729–737. https://doi.org/10.1242/jcs.102.4.729.

26. Ma, K., Luo, M., Xie, G., Wang, X., Li, Q., Gao, L., Yu, H., and Yu, X. (2022). Ribosomal RNA regulates chromosome clustering during mitosis. Cell Discov. *8*, 51. https://doi.org/10.1038/s41421-022-00400-7.

27. Takagi, M., Sueishi, M., Saiwaki, T., Kametaka, A., and Yoneda, Y. (2001). A novel nucleolar protein, NIFK, interacts with the forkhead associated domain of Ki-67 antigen in mitosis. J. Biol. Chem. *276*, 25386–25391. https://doi.org/10.1074/jbc.M102227200.

28. Van Hooser, A.A.V., Yuh, P., and Heald, R. (2005). The perichromosomal layer. Chromosoma *114*, 377–388. https://doi.org/10.1007/s00412-005-0021-9.

29. Booth, D.G., Beckett, A.J., Molina, O., Samejima, I., Masumoto, H., Kouprina, N., Larionov, V., Prior, I.A., and Earnshaw, W.C. (2016). 3D-CLEM Reveals that a Major Portion of Mitotic Chromosomes Is Not Chromatin. Mol. Cell *64*, 790–802. https://doi.org/10.1016/j.molcel.2016.10.009.

30. Pak, C.W., Kosno, M., Holehouse, A.S., Padrick, S.B., Mittal, A., Ali, R., Yunus, A.A., Liu, D.R., Pappu, R.V., and Rosen, M.K. (2016). Sequence Determinants of Intracellular Phase Separation by Complex Coacervation of a Disordered Protein. Mol. Cell *63*, 72–85. https://doi.org/10.1016/j.molcel.2016.05.042.

31. Boeynaems, S., Holehouse, A.S., Weinhardt, V., Kovacs, D., Van Lindt, J., Larabell, C., Van Den Bosch, L., Das, R., Tompa, P.S., Pappu, R.V., and Gitler, A.D. (2019). Spontaneous driving forces give rise to protein–RNA condensates with coexisting phases and complex material properties. Proc. Natl. Acad. Sci. USA *116*, 7889–7898. https://doi.org/10.1073/pnas.1821038116.

32. Quail, T., Golfier, S., Elsner, M., Ishihara, K., Murugesan, V., Renger, R., Jülicher, F., and Brugués, J. (2021). Force generation by protein–DNA co-condensation. Nat. Phys. *17*, 1007–1012. https://doi.org/10.1038/s41567-021-01285-1.

33. Keenen, M.M., Brown, D., Brennan, L.D., Renger, R., Khoo, H., Carlson, C.R., Huang, B., Grill, S.W., Narlikar, G.J., and Redding, S. (2021). HP1 proteins compact DNA into mechanically and positionally stable phase separated domains. eLife *10*, e64563. https://doi.org/10.7554/eLife.64563.

34. Renger, R., Morin, J.A., Lemaitre, R., Ruer-Gruss, M., Jülicher, F., Hermann, A., and Grill, S.W. (2022). Co-condensation of proteins with single- and double-stranded DNA. Proc. Natl. Acad. Sci. USA *119*, e2107871119. https://doi.org/10.1073/pnas.2107871119.

35. Shin, Y., Chang, Y.-C., Lee, D.S.W., Berry, J., Sanders, D.W., Ronceray, P., Wingreen, N.S., Haataja, M., and Brangwynne, C.P. (2018). Liquid Nuclear Condensates Mechanically Sense and Restructure the Genome. Cell *175*, 1481–1491.e13. https://doi.org/10.1016/j.cell.2018.10.057.

36. de Gennes, P.-G., Brochard-Wyart, F., and Quéré, D. (2004). Capillarity and Wetting Phenomena, Drops, Bubbles, Pearls, Waves (Springer), pp. 1–31. https://doi.org/10.1007/978-0-387-21656-0_1.

37. Steinberg, M.S. (1996). Adhesion in Development: An Historical Overview. Dev. Biol. *180*, 377–388. https://doi.org/10.1006/dbio.1996.0312.

38. Hayashi, T., and Carthew, R.W. (2004). Surface mechanics mediate pattern formation in the developing retina. Nature *431*, 647–652. https://doi.org/10.1038/nature02952.

39. Gouveia, B., Kim, Y., Shaevitz, J.W., Petry, S., Stone, H.A., and Brangwynne, C.P. (2022). Capillary forces generated by biomolecular condensates. Nature *609*, 255–264. https://doi.org/10.1038/s41586-022-05138-6.

40. Broyles, B.K., Gutierrez, A.T., Maris, T.P., Coil, D.A., Wagner, T.M., Wang, X., Kihara, D., Class, C.A., and Erkine, A.M. (2021). Activation of gene expression by detergent-like protein domains. Iscience *24*, 103017. https://doi.org/10.1016/j.isci.2021.103017.

41. Kelley, F.M., Favetta, B., Regy, R.M., Mittal, J., and Schuster, B.S. (2021). Amphiphilic proteins coassemble into multiphasic condensates and act as biomolecular surfactants. Proc. Natl. Acad. Sci. USA *118*, e2109967118. https://doi.org/10.1073/pnas.2109967118.

42. Folkmann, A.W., Putnam, A., Lee, C.F., and Seydoux, G. (2021). Regulation of biomolecular condensates by interfacial protein clusters. Science *373*, 1218–1224. https://doi.org/10.1126/science.abg7071.

43. Cidado, J., Wong, H.Y., Rosen, D.M., Cimino-Mathews, A., Garay, J.P., Fessler, A.G., Rasheed, Z.A., Hicks, J., Cochran, R.L., Croessmann, S., et al. (2016). Ki-67 is required for maintenance of cancer stem cells but not cell proliferation. Oncotarget *7*, 6281–6293. https://doi.org/10.18632/oncotarget.7057.

44. Sobecki, M., Mrouj, K., Camasses, A., Parisis, N., Nicolas, E., Llères, D., Gerbe, F., Prieto, S., Krasinska, L., David, A., et al. (2016). The cell proliferation antigen Ki-67 organises heterochromatin. eLife *5*, e13722. https://doi.org/10.7554/eLife.13722.

45. Lukinavičius, G., Blaukopf, C., Pershagen, E., Schena, A., Reymond, L., Derivery, E., Gonzalez-Gaitan, M., D'Este, E., Hell, S.W., Wolfram Gerlich, D.W., and Johnsson, K. (2015). SiR–Hoechst is a far-red DNA stain for live-cell nanoscopy. Nat. Commun. *6*, 8497. https://doi.org/10.1038/ncomms9497.

46. Gaspar, I., Wippich, F., and Ephrussi, A. (2017). Enzymatic production of single-molecule FISH and RNA capture probes. RNA *23*, 1582–1591. https://doi.org/10.1261/rna.061184.117.

47. Carron, C., O'Donohue, M.-F., Choesmel, V., Faubladier, M., and Gleizes, P.-E. (2011). Analysis of two human pre-ribosomal factors, bystin and hTsr1, highlights differences in evolution of ribosome biogenesis between yeast and mammals. Nucleic Acids Res. *39*, 280–291. https://doi.org/10.1093/nar/gkq734.

48. Sommer, C., Hoefler, R., Samwer, M., and Gerlich, D.W. (2017). A deep learning and novelty detection framework for rapid phenotyping in high-content screening. Mol. Biol. Cell *28*, 3428–3436. https://doi.org/10.1091/mbc.E17-05-0333.

49. Thompson, A.P., Aktulga, H.M., Berger, R., Bolintineanu, D.S., Brown, W.M., Crozier, P.S., in 't Veld, P.J., Kohlmeyer, A., Moore, S.G., Nguyen, T.D., et al. (2022). LAMMPS - a flexible simulation tool for particle-based materials modeling at the atomic, meso, and continuum scales. Comput. Phys. Commun. *271*, 108171. https://doi.org/10.1016/j.cpc.2021.108171.

50. Erdős, G., Pajkos, M., and Dosztányi, Z. (2021). IUPred3: prediction of protein disorder enhanced with unambiguous experimental annotation and visualization of evolutionary conservation. Nucleic Acids Res. *49*, W297–W303. https://doi.org/10.1093/nar/gkab408.

51. Schindelin, J., Arganda-Carreras, I., Frise, E., Kaynig, V., Longair, M., Pietzsch, T., Preibisch, S., Rueden, C., Saalfeld, S., Schmid, B., et al. (2012). Fiji: an open-source platform for biological-image analysis. Nat. Methods *9*, 676–682. https://doi.org/10.1038/nmeth.2019.

52. Schmitz, M.H.A., Held, M., Janssens, V., Hutchins, J.R.A., Hudecz, O., Ivanova, E., Goris, J., Trinkle-Mulcahy, L., Lamond, A.I., Poser, I., et al. (2010). Live-cell imaging RNAi screen identifies PP2A-B55[alpha] and importin-[beta]1 as key mitotic exit regulators in human cells. Nat. Cell Biol. *12*, 886–893. https://doi.org/10.1038/ncb2092.

53. Politi, A.Z., Cai, Y., Walther, N., Hossain, M.J., Koch, B., Wachsmuth, M., and Ellenberg, J. (2018). Quantitative mapping of fluorescently tagged cellular proteins using FCS-calibrated four-dimensional imaging. Nat. Protoc. *13*, 1445–1464. https://doi.org/10.1038/nprot.2018.040.

54. Berg, S., Kutra, D., Kroeger, T., Straehle, C.N., Kausler, B.X., Haubold, C., Schiegg, M., Ales, J., Beier, T., Rudy, M., et al. (2019). ilastik: interactive machine learning for (bio)image analysis. Nat. Methods *16*, 1226–1232. https://doi.org/10.1038/s41592-019-0582-9.

55. Kremer, K., and Grest, G.S. (1990). Dynamics of entangled linear polymer melts: A molecular-dynamics simulation. J. Chem. Phys. *92*, 5057–5086. https://doi.org/10.1063/1.458541.

56. Svaneborg, C., and Everaers, R. (2020). Characteristic Time and Length Scales in Melts of Kremer–Grest Bead–Spring Polymers with Wormlike Bending Stiffness. Macromolecules *53*, 1917–1941. https://doi.org/10.1021/acs.macromol.9b02437.

57. Schneider, T., and Stoll, E. (1978). Molecular-dynamics study of a three-dimensional one-component model for distortive phase transitions. Phys. Rev. B *17*, 1302–1322. https://doi.org/10.1103/PhysRevB.17.1302.

58. Plimpton, S. (1995). Fast Parallel Algorithms for Short-Range Molecular Dynamics. J. Comput. Phys. *117*, 1–19. https://doi.org/10.1006/jcph.1995.1039.

## STAR★METHODS

### KEY RESOURCES TABLE

| REAGENT or RESOURCE | SOURCE | IDENTIFIER |
|---|---|---|
| Antibodies | | |
| Rabbit Monoclonal Anti-Ki-67 | Abcam | RRID:AB_302459 |
| Goat Anti-Rabbit IgG, Alexa Fluor™ 594 | Thermo Fisher Scientific | RRID:AB_2534095 |
| Bacterial and virus strains | | |
| MegaX DH10B $T1^R$ Electrocomp™ Cells | Thermo Fisher Scientific | Cat#C640003 |
| Chemicals, peptides, and recombinant proteins | | |
| DMEM | Thermo Fisher Scientific | Cat#41965039 |
| FBS | Thermo Fisher Scientific | Cat#10270106 |
| Penicillin-Streptomycin | Thermo Fisher Scientitic | Cat#15140122 |
| Sodium pyruvate | Thermo Fisher Scientific | Cat#11360039 |
| SiR-Hoechst | Lukinavičius et al.[45] | N/A |
| FluoroBrite™ DMEM | Thermo Fisher Scientific | Cat#A1896701 |
| GlutaMAX™ | Thermo Fisher Scientific | Cat#35050038 |
| Trypsin-EDTA | Thermo Fisher Scientific | Cat#25200056 |
| Polyethylenimine Max (PEI MAX®) | Polysciences | Cat#24765-1 |
| Nocodazole | Sigma-Aldrich | CAS: 31430-18-9 |
| Flavopiridol hydrochloride | Tocris Bioscience | CAS: 131740-09-5 |
| Actinomycin D | Thermo Fisher Scientific | Cat#11805017 |
| α-Amanitin | Sigma-Aldrich | Cat#A2263 |
| BMH-21 | Sigma-Aldrich | CAS: 896705-16-1 |
| Thymidine | Sigma-Aldrich | CAS: 50-89-5 |
| 5-Ethynyl Uridine (EU) | Thermo Fisher Scientific | Cat#E10345 |
| Formaldehyde | Sigma-Aldrich | CAS: 50-00-0 |
| Triton® X-100 | Roth | CAS: 9002-93-1 |
| Bovine Serum Albumin (BSA) | Sigma-Aldrich | CAS: 9048-46-8 |
| DAPI | Thermo Fisher Scientific | Cat#62248 |
| Formamide | Sigma-Aldrich | CAS: 75-12-7 |
| Sodium citrate tribasic dihydrate | Merck | CAS: 6132-04-3 |
| Dextran sulfate | Merck | Cat#S4030 |
| Ribonucleoside-vanadyl complex | New England Biolabs | Cat#S1402S |
| Paclitaxel (taxol) | Sigma-Aldrich | CAS: 33069-62-4 |
| Glycerol | Merck | 1.04092.2511 |
| $Mg(OAc)_2$ | Merck | M5661 |
| CF®680R-Dextran 10000-MW | VWR | 80116 |
| STLC | Merck | 164739 |
| RNase A | Thermo Fisher Scientific | EN0531 |
| Critical commercial assays | | |
| Click-iT™ Plus Alexa Fluor™ 647 Picolyl Azide Toolkit | Thermo Fisher Scientific | Cat#C10643 |
| Deposited data | | |
| Raw microscopy images | This study | Mendeley Data 10.17632/dwcpnncsyd.1 |
| Experimental models: Cell lines | | |
| HeLa Kyoto Ki-67 KO | Published in Cuylen et al.[8] | Lab ID c-63 |
| HeLa Kyoto Wild-type | Originally from S. Narumiya (Kyoto University, Japan) | Lab ID c-1 |
| HeLa Kyoto EGFP-MKI67 (homozygous) | Published in Cuylen et al.[8] | Lab ID c-77 |

(*Continued on next page*)

*Continued*

| REAGENT or RESOURCE | SOURCE | IDENTIFIER |
|---|---|---|
| HeLa Kyoto Ki-67 KO (RIEP), BAF-TagRFP | Gift from Gerlich lab (IMBA, Austria) | Lab ID c-116 |
| HeLa Kyoto Ki-67 KO (RIEP), mCherry-Lap2beta | Gift from Gerlich lab (IMBA, Austria) | Lab ID c-115 |
| HeLa Kyoto Ki-67 KO (RIEP), TagRFP-LaminB1 | Gift from Gerlich lab (IMBA, Austria) | Lab ID c-117 |
| HeLa Kyoto EGFP-MKI67(RASA) (homozygous) | Gift from Gerlich lab (IMBA, Austria) | Lab ID c-102 |
| HeLa Kyoto mCherry-MKI67 (homozygous) | This study | Lab ID c-149 |
| HeLa Kyoto Ki-67 KO, GEM-EGFP, H2B-mCherry | Gift from Gerlich lab (IMBA, Austria) | Lab ID c-171 |
| HeLa Kyoto GEM-EGFP, H2B-mCherry (RIEP) | Gift from Gerlich lab (IMBA, Austria) | Lab ID c-169 |
| **Oligonucleotides** | | |
| Oligo(dT): 5′-TTTTTTTTTTTTTTTTTTTT TTTTTTTT3′-Atto633 | Gaspar et al.[46] | N/A |
| ETS1: Cy3-5′CGCTAGAGAAGGCTTTTCTC3′-Cy3 | Carron et al.[47] | N/A |
| **Recombinant DNA** | | |
| EGFP-Ki-67 | This study | Lab ID p-343 |
| EGFP-Ki-67ΔLR | This study | Lab ID p-428 |
| EGFP-LR | This study | Lab ID p-726 |
| Ki-67ΔLR-mNeonGreen | This study | Lab ID p-190 |
| EGFP-Ki-67(139E) | This study | Lab ID p-318 |
| EGFP-Ki-67(139E)ΔLR | This study | Lab ID p-429 |
| EGFP-Ki-67(139D) | This study | Lab ID p-1005 |
| EGFP-Ki-67(139D)ΔLR | This study | Lab ID p-1242 |
| EGFP-N term | This study | Lab ID p-435 |
| EGFP-Ki-67ΔN term | This study | Lab ID p-665 |
| EGFP-Ki-67ΔRepeats | This study | Lab ID p-607 |
| EGFP-Ki-67ΔCP | This study | Lab ID p-483 |
| EGFP-Ki-67ΔFASI | This study | Lab ID p-666 |
| EGFP-Ki-67(C termΔLR) | This study | Lab ID p-434 |
| EGFP-N termΔCP | This study | Lab ID p-475 |
| EGFP-N termΔFASI | This study | Lab ID p-439 |
| EGFP-Ki-67(CP(RK→A)) | This study | Lab ID p-744 |
| EGFP-Ki-67ΔCP-strict | This study | Lab ID p-490 |
| EGFP-N term(CP(RK→A)) | This study | Lab ID p-986 |
| EGFP-N termΔCP-strict | This study | Lab ID p-484 |
| EGFP-Ki-67(129E) | This study | Lab ID p-537 |
| EGFP-Ki-67(129E)ΔLR | This study | Lab ID p-991 |
| mCherry-Ki-67-EGFP | This study | Lab ID p-216 |
| mCherry-Ki-67(139E)-EGFP | This study | Lab ID p-825 |
| mCherry-Ki-67(129E)-EGFP | This study | Lab ID p-922 |
| EGFP-Ki-67ΔLR-H2B | This study | Lab ID p-711 |
| EGFP-CP-Repeats-LR | This study | Lab ID p-818 |
| EGFP-N term(RASA) | This study | Lab ID p-936 |
| mCherry-Ki-67 | This study | Lab ID p-339 |
| mCherry-Ki-67(139E) | This study | Lab ID p-817 |
| **Software and algorithms** | | |
| Zen 2011 | Zeiss | https://www.zeiss.com/microscopy/en/products/software/zeiss-zen.html |
| CellCognition Explorer | Sommer et al.[48] | https://software.cellcognition-project.org/ |
| LAMMPS | Thompson et al.[49] | =https://www.lammps.org/#gsc.tab=0 |

(*Continued on next page*)

*Continued*

| REAGENT or RESOURCE | SOURCE | IDENTIFIER |
|---|---|---|
| EMBOSS Charge webtool | Written by Alan Bleasby | https://www.bioinformatics.nl/cgi-bin/emboss/charge |
| SEG webtool | Wootton et al.[21] | https://mendel.imp.ac.at/METHODS/seg.server.html |
| IUPred3 | Erdős et al.[50] | https://iupred3.elte.hu |
| Fiji/ImageJ version 2.1.0/1.53c and version 1.47n | Schindelin et al.[51] | https://imagej.net/software/fiji/ |
| R Studio 1.1.453 R version 3.6.1 | Open Source | https://posit.co/download/rstudio-desktop/ https://www.R-project.org/ |
| Graph Pad Prism 10 | GraphPad | https://www.graphpad.com/ |
| Simulation code | This study | Github: https://github.com/Saric-Group/chromosome_clustering.git Zenodo: https://doi.org/10.5281/zenodo.12706119 |
| Fiji and R codes | This study | Github: https://github.com/CuylenLab/Armendariz_et_al_2024 |

## RESOURCE AVAILABILITY

### Lead contact

Further information and requests for resources and reagents should be directed to and will be fulfilled by the lead contact, Sara Cuylen-Haering (sara.cuylen-haering@embl.de).

### Materials availability

All unique materials generated in this study will be made available on request from the lead contact upon completion of a Materials Transfer Agreement.

### Data and code availability

- Raw image files of all figures have been deposited at Mendeley Data and are publicly available as of the date of publication (Mendeley data: https://doi.org/10.17632/dwcpnncsyd.1). All other data reported in this paper will be shared by the lead contact upon request.
- All original code has been deposited at GitHub (for simulation code see Github: https://github.com/Saric-Group/chromosome_clustering.git and Zenodo: https://doi.org/10.5281/zenodo.12706119 and for Fiji and R scripts see Github: https://github.com/CuylenLab/Armendariz_et_al_2024).
- Any additional information required to reanalyze the data reported in this paper is available from the lead contact upon request.

## EXPERIMENTAL MODEL AND STUDY PARTICIPANT DETAILS

### Human cell lines

All cell lines were regularly verified negatively for mycoplasma contamination with Mycoplasma PCR Detection Kit (abm, G238) and listed in the key resources table. All HeLa cell lines were derived from a HeLa *Kyoto* cell line described in Schmitz et al.[52] HeLa wild-type cells are female and were validated by a Multiplex human Cell Authentication test (MCA). Cells were cultured in Dulbecco's modified medium (DMEM; Gibco, 41965039) containing 10% (v/v) fetal bovine serum (FBS; Gibco, 10270106), 1% (v/v) penicillin-streptomycin (Sigma Aldrich, 15140122) and 1 mM sodium pyruvate (Gibco, 11360039) and passaged every 2 – 3 days using 0.25% Trypsin-EDTA (Gibco, 25200056). DNA was visualized by labelling with 100 nM SiR-Hoechst[45] unless otherwise indicated. Live cell imaging was performed in FluoroBrite™ DMEM (Gibco, A1896701) containing 10% (v/v) FBS, 1% (v/v) penicillin-streptomycin, 1% (v/v) GlutaMAX (Gibco, 35050038) and 1 mM sodium pyruvate. Cells were grown in LabTek chambered coverglass (Thermo Scientific).

## METHOD DETAILS

### Generation of Ki-67 constructs

All constructs are listed in the key resources table. Regions within Ki-67 (3256 total amino acids) were defined as follows: N terminus (1 – 1002); C terminusΔLR (also called Repeats) (1003 – 2929); LR domain (2930 – 3256); FASI (136 – 495); Charged Patch

(CP) (496 – 681); Charged Patch-strict (CP-strict) (571 – 647). Ki-67(139E) was generated by Gibson assembly of three gBlocks (IDT) into an IRESpuro2 backbone. Ki-67(139D) was generated by gene synthesis and cloned into an IRESpuro2 backbone containing CMV promoter and the LR domain.

### Plasmid transfections

Transfections were done transiently using PEI transfection reagent (1 mg $ml^{-1}$ stock, Polysciences, 24765-1), 4 μg of transfection reagent per 1 μg of plasmid, and incubated for 48 h before imaging.

### Inhibitors and stains

Cells were arrested in prometaphase by incubating them for 2 – 4 h in 200 ng $ml^{-1}$ nocodazole (Sigma-Aldrich, 31430-18-9). Mitotic exit was induced by adding flavopiridol (Tocris Bioscience, 131740-09-5) to a final concentration of 20 μM. All drug treatments were performed for 3 – 5 h before imaging with a final concentration of 5 nM of actinomycin D (Gibco, 11805-017), 50 μg/mL of alpha-amanitin (Sigma-Aldrich, A2263), or 1 μM of BMH-21 (Sigma-Aldrich, 896705-16-1).

### RNA visualization and Ki-67 immunofluorescence

HeLa wild-type cells and HeLa Ki-67 KO cells were co-seeded in single wells and synchronized by a double thymidine block. Specifically, cells were incubated for 24 h in a medium containing 2 mM thymidine (Sigma-Aldrich, 50-89-5), followed by their release in fresh medium. After 8 h, the medium was exchanged for 2 mM thymidine-containing medium and incubated for 16 h. Afterwards, the medium was exchanged for fresh medium and incubated for 6 h. Then, cells were incubated in a medium containing 200 μM of 5-Ethynyl Uridine (Thermo Fisher Scientific, E10345) and after 3 h, cells were washed with PBS and fixed with 4% PFA (Merck, 50-00-0) for 15 min at room temperature. Afterwards, the fixed cells were washed twice with PBS and permeabilized with 0.2 % Triton X-100 (Roth, 9002-93-1) for 5 min at room temperature, followed by two washes with 3 % BSA (Sigma-Aldrich, 9048-46-8). For labeling, fixed cells were treated with Click-iT™ Plus (Invitrogen, C10643) reaction cocktail for 30 min in the dark, washed twice with 3 % BSA and incubated for 1 h with monoclonal rabbit anti-Ki-67 antibody (Abcam, ab16667, 1:1000) and washed three times with PBS. Alexa 594 goat anti-rabbit IgG (Invitrogen, A11037, 1:500) was used for visualization, incubated for 45 min and washed three times with PBS. Finally, DNA was incubated with DAPI (Thermo Fisher Scientific, 62248, 1:1000) for 5 min and washed once with PBS.

### RNA-FISH of mRNAs and pre-rRNAs

Homozygous endogenously EGFP-labelled Ki-67 HeLa cells or HeLa Ki-67 KO cells were seeded and synchronized by a double thymidine block (see above). After 6 h of the second thymidine release, cells were either untreated or treated with actinomycin D or BMH-21. After 3 h, cells were fixed and permeabilized as previously described. Afterwards, cells were washed three times with PBS for 5 min, incubated with wash buffer (10 % formamide (Sigma-Aldrich, 75-12-7) in 2× saline sodium citrate (SSC; Merck, 6132-04-3)) for 5 min at room temperature. Then, the solution was exchanged to hybridization buffer (10% formamide, 2× SSC, 10% dextran sulfate (Merck, S4030), 10 mM ribonucleoside-vanadyl complex (NEB, S1402S)) supplemented with 125 nM probe (Oligo(dT)30 labelled with Atto-633 on the 3′ end[46] or ETS1-1399 (Cy35′CGCTAGAGAAGGCTTTTCTC3′Cy3[47]) and incubated overnight at 37°C in a humidified chamber. Cells were gently washed twice with wash buffer in the dark for 15 min at 37°C. DNA was labelled with DAPI (Thermo Fisher Scientific, 62248, 1:1000) at room temperature for 5 min and washed twice with PBS.

### Microscopy

Imaging was performed on a customized confocal Zeiss LSM780 microscope, using × 40 or × 63, 1.4 NA, Oil DIC Plan-Apochromat objective (Zeiss), operated by ZEN 2011 software, and an incubator chamber (European Molecular Biology Laboratory (EMBL), Heidelberg, Germany) provided constant humidity and 37°C temperature with 5% $CO_2$.

### Microinjection

Live-cell microinjection experiments were performed using a FemtoJet microinjector (Eppendorf, 5181000017) in conjunction with an InjectMan NI2 micromanipulation device (Eppendorf, 5247000013). All microinjections were performed using pre-pulled Femtotips injection capillaries (Eppendorf, 5242952008). The microinjection device was directly mounted onto a customized confocal Zeiss LSM780 as described above.

Homozygous endogenously EGFP-labelled Ki-67 HeLa cells were cultured in μ-Dish 35 mm high-wall imaging dishes with a polymer bottom (ibidi, 81156) to reach 80%–90% confluency on the day of the injection. Cells were synchronized in mitosis for 2 – 4 h with 10 μM (+)-S-Trityl-L-cysteine (STLC) (Sigma, 164739) and DNA was stained with 0.2 μM SiR-DNA (Spirochrome, SC007). RNase A (Thermo Scientific, EN0531) stock solution was diluted to 100 ng/ml in microinjection buffer (50 mM HEPES pH 7.4 (homemade), 5% glycerol (Merck, 1.04092.2511), 1 mM $Mg(OAc)_2$ (Sigma, M5661)) supplemented with 1 mg/ml CF®680R-condjugated 10k-MW dextran (VWR, 80116). Using an Eppendorf Microcapillary Microloader (Eppendorf, 5242956003), 4 – 6 μl diluted RNase A was loaded into a Femtotip. Microinjection was performed using injection settings of 150 hPa injection pressure, 0.2 s injection time and 30 hPa compensation pressure. After 10 – 15 minutes of injection, flavopiridol was added to a final concentration of 20 μM, and cells were imaged 7 – 11 min later to assess Ki-67 condensate formation and enrichment to chromosomes.

### Quantification of areas and enrichments

Maximum intensity projections (4 z-sections with 2 μm spacing) of cells expressing EGFP- or mCherry-tagged proteins were analyzed using CellCognition Explorer,[48] where a primary segmentation mask in the chromatin channel was defined by applying a local adaptive threshold, and both channels quantified. Using R, the signals were normalized to the mean value before flavopiridol addition for each cell.

Similarly, RNA was quantified in central single z-slices using CellCognition Explorer,[48] where DAPI-labelled chromosomes were segmented with a primary segmentation mask and the cytoplasm by a rim of 5 pixels surrounding each segmented set of chromosomes using the Ring function (inner distance, 15; outer distance, 20). Using R, the chromosome signals were divided by their corresponding cytoplasmic signals, and normalized to the average value of Ki-67 KO cells undergoing metaphase in Figure 6B, and to the average value of Control cells undergoing metaphase in Figures S5B and S5D.

### Quantification of GEMs in chromosome ensemble area

Quantification of GEMs was done in Fiji[51] by segmenting the chromosome ensemble area in a single central z-slice (4 z-sections with 2 μm spacing). If bleaching was observed, a frame-wise exponential fitting using the Image J plug-in "Bleach correction" (htt://fiji.sc/Bleach_Correction) was performed before segmentation. The bleached-corrected chromatin channel of the central single z-slice was denoised using a Gaussian blur filter ($\sigma = 2$) and thresholded using ImageJ's default method (a variation of the IsoData algorithm) and converted to a binary image. Next, the Fiji convex hull algorithm (https://blog.bham.ac.uk/intellimic/g-landini-software/) was applied to the binary image and used as a mask for the quantification of GEM fluorescence intensity in the chromosome ensemble area of the central single z-slices. All cells were normalized to the average GEM total fluorescence (in the chromosome ensemble area) before flavopiridol addition.

### Quantification of cytoplasmic condensates

To only measure cytoplasmic Ki-67, a chromosome mask was generated based on SiR-Hoechst images and used to cancel any Ki-67 signal in that area. In detail, the chromosome area was segmented in maximum intensity z-projections of SiR-Hoechst images (4 z-sections with 2 μm spacing) which were denoised using Gaussian blur ($\sigma = 2$), thresholded using ImageJ's default automated method and converted to a binary image. This mask was dilated with 20 iterations, to avoid any fluorescent signal originating from the chromosome ensemble area, and inverted resulting in 0 values for the chromosome mask. To quantify the number of condensates in the cytoplasm only, the inverted mask was multiplied with the GFP channel cancelling any GFP signal in the chromosome area. The GFP image was denoised using Gaussian blur ($\sigma = 2$) and the background was subtracted using the "subtract background" function with a 25-pixel rolling ball radius. The threshold was set to (0, 2500) for all N terminus and full-length mutants tested, and to (0, 2000) and (0, 1000) for quantification of endogenously tagged EGFP- and mCherry-Ki-67 cell lines, respectively. In addition, a frame-wise exponential fitting using the Image J plug-in "Bleach correction" (htt://fiji.sc/Bleach_Correction) was performed before condensate segmentation for mCherry-Ki-67 expressing cells. The respective image was transformed into a mask and the function "Analyze particles" was used to quantify the number of condensates and the sum of their areas per frame.

### Quantification of absolute Ki-67 concentration

To quantify absolute concentrations of Ki-67 during mitotic exit in living cells, fluorescence correlation spectroscopy (FCS)-calibrated imaging was performed as in Politi et al.[53] In brief, HeLa Kyoto cells were either untransfected (for estimation of background photon counts) or transfected with mEGFP (for FCS measurements of freely diffusing mEGFP) 24 h before imaging. HeLa EGFP-Ki-67 knockin cells[8] were seeded 48 h prior to imaging.

The acquisition was carried out on a Zeiss LSM880 using a C-Apochromat × 40, 1.20 NA, W Korr FCS M27 water-immersion objective. Confocal volume estimation was carried out by ten FCS measurements of 1 min of 10 nM Atto488 (AD 488-21, ATTO-TEC) in double-distilled water. Of note, Atto488 carboxylic acid was used for the effective confocal volume measurement instead of the previously reported AF488-NHS.[53] Use of the Atto488 dye in combination with its reported diffusion coefficient of 400 $\mu m^2/s$ at 25°C (PicoQuant) typically results in larger effective confocal volume estimates and therefore lower absolute concentrations compared to AF488-NHS.[53] Background fluorescence and background photon counts were determined by FCS measurements targeted to both the nucleus and cytoplasm of untransfected HeLa Kyoto cells. Subsequently, repeated imaging and nuclear and cytoplasmic FCS measurements of cells expressing a broad range of mEGFP were recorded. In combination with the estimated effective confocal volume, an experiment-specific internal calibration factor was computed with which measured mEGFP fluorescence intensities could be converted into protein concentrations in any image that was acquired with the same imaging settings.

Mitotic exit movies of unsynchronized EGFP-Ki-67 knockin cells were acquired by automated detection of metaphase cells in large fields of view using low-resolution imaging of the SiR-Hoechst channel and ilastik-based image segmentation and classification,[54] followed by high-resolution imaging every minute for 40 min.

Quantification of fluorescence intensities was performed in single-z slices using Fiji. Cytoplasmic condensates were segmented as described above. For chromosomes, a mask was generated based on SiR-Hoechst images and used to measure the Ki-67 signal in that area. Specifically, the chromosome area was segmented, denoised using Gaussian blur ($\sigma = 2$), thresholded using ImageJ's default automated method, converted to a binary image, and dilated with 5 iterations. Next, the GFP image was denoised using Gaussian blur ($\sigma = 2$) and background-subtracted with a 25-pixel rolling ball radius. Then, thresholded to (0, 5000) and the respective

images were transformed into a mask and the function ''Analyze particles'' was used to quantify the intensities. For quantifying the cytoplasmic fluorescence intensity, a circular ROI (1.5 μm of diameter), was used to follow the fluorescence of the cytoplasm over time.

### FRAP measurements

EGFP-labelled Ki-67ΔLR was transiently transfected to Ki-67 KO cells and spindle-less mitotic exit was induced as previously described. Six min after flavopiridol addition, a pre-bleach time series was acquired for at least 9 s. A circular ROI (diameter between 0.5 to 1.0 μm) was used for partially bleaching condensates of at least 1 μm in diameter. To capture recovery, time series of at least 60 s were acquired with 0.5 s intervals. Similarly, for addressing the mobility of Ki-67's chromosome-bound pool, a circular ROI (diameter of 2 μm) was used for bleaching EGFP-Ki-67 knockin cells chromosomes, previous to flavopiridol addition and after 3 min. Both conditions, considered pre-bleach time series for at least 9 s and the recovery of fluorescence was followed for at least 3 min with 0.5 s intervals.

### Quantification of Ki-67's molecular extension

To measure Ki-67 molecular extension at the chromosome surface, both termini of Ki-67 were tagged with different fluorescent proteins and Gaussian functions were fitted to their line profiles as described in Stenström et al.[4] and Hernandez-Verdun and Gautier.[5] Ki-67 KO cells were transfected with either mCherry-Ki-67-EGFP, mCherry-Ki-67(139E)-EGFP or mCherry-Ki-67(129E)-EGFP, arrested in a medium containing 0.5 μM taxol (Sigma, T1912) for 1 h and recorded before and 5 – 8 min after flavopiridol addition. Only chromosomes with their arms oriented perpendicular to the imaging plane were analyzed, by measuring line profiles of red and green channels that sectioned a single sister chromatid. After background subtraction and normalization to total fluorescence intensity, the sum of two Gaussian functions was fitted and the distance between the Gaussian center positions was measured separately for green and red fluorescent channels using R. This value represents the sum of both chromatic shifts perpendicular to the chromosome surface and the molecular extension of Ki-67 can be calculated by dividing this value by two.

### Ki-67 orthologues

Ki-67 sequences were obtained from NCBI: *Homo sapiens* (NP_002408.3), *Mus musculus* (NP_001074586.2), *Rattus norvegicus* (NP_001258295.1), *Xenopus laevis* (NP_001128553.1), *Danio rerio* (NP_001264375.1).

### Coarse-grained model

To model the dispersion and clustering of chromosomes in the presence of Ki-67 and RNA, we perform *NVT* (constant number of particles, volume, and temperature) molecular dynamics (MD) simulations of a coarse-grained model. Chromosome surfaces are modeled as rigid bodies, generated by arranging spherical beads of diameter $\sigma$ on a surface (either a surface or a half cylinder, see below). In experimental units, $\sigma \simeq 12$ nm (see discussion about units conversion below). The bead surface number density is $\rho_s = \sigma^{-2}$.

Ki-67 molecules can be either grafted to the chromosome surfaces or free (the latter molecules modeling cytoplasmic Ki-67). Each molecule is modeled as a bead-spring polymer chain of $N_{\mathrm{Ki67}} = 24$ beads (bead diameter = $\sigma$). The grafted molecules are bound to the chromosome surface by finite extensible nonlinear elastic (FENE) bonds (see Equation 4 below), *i.e.*, the LR domain and its interaction with the chromosome is not modeled explicitly. RNA molecules are also modeled as bead-spring polymer chains of $N_{\mathrm{RNA}} = 100$ beads (bead diameter = $\sigma$) which can freely move in the simulation box. To investigate the role of RNA in chromosome clustering, we have also considered systems without RNA.

The interaction between all the beads (belonging to the chromosomes, to the Ki-67 and to the RNA) is modeled by an excluded volume component $E_{\mathrm{exc.vol}}$ (truncated and shifted Lennard-Jones potential), which models steric interactions, and a screened electrostatic component $E_{\mathrm{el}}$. The total interaction potential is thus

$$E_{\mathrm{tot}}(r) = \begin{cases} E_{\mathrm{exc.vol}}(r) + E_{el}(r) & r < r_{\mathrm{exc.vol}} \\ E_{\mathrm{el}}(r) & r_{\mathrm{exc.vol}} \leq r < r_{\mathrm{el}} \\ 0 & r_{el} \leq r \end{cases} \quad \text{(Equation 1)}$$

where $r$ is the distance between the centers of the beads and the two interaction potentials are given by

$$E_{\mathrm{exc.vol}}(r) = 4\epsilon\left[\left(\frac{\sigma}{r}\right)^{12} - \left(\frac{\sigma}{r}\right)^{6}\right] + \epsilon \quad \text{(Equation 2)}$$

$$E_{\mathrm{el}}(r) = \frac{C q_i q_j}{\epsilon_d r} e^{-r/\lambda} \quad \text{(Equation 3)}$$

and $r_{\mathrm{exc.vol}} = 2^{1/6}\sigma$, $r_{\mathrm{el.}} = 3\sigma$ are the cutoff lengths of the two potentials. In Equation 2, $\epsilon$ is the interaction energy. In Equation 3, $C$ is a unit conversion constant, $q_i, q_j$ are the charges of the two interacting particles, $\epsilon_d = 5.0$ is the dielectric constant and $\lambda = \sigma/2$ is the

Debye screening length. In what follows, we use MD reduced units ($\epsilon = 1$, $\sigma = 1$, $k_B = 1$ and $m = 1$, with $m$ the mass of the beads comprising the Ki-67 and RNA polymers). All the other quantities will be expressed in these MD reduced units unless explicitly stated.

Bonded neighbors in the same polymer chain interact only via the excluded volume term Equation 2, plus an additional finite extensible nonlinear elastic (FENE) potential:

$$U_{\mathrm{FENE}}(r) = -\frac{Kr_0^2}{2}\ln\left[1-(r/r_0)^2\right] \quad \text{(Equation 4)}$$

with $K = 30$ and $r_0 = 1.5$ (Kremer-Grest model[55]). These values are chosen in such a way to prevent chain-crossing. In addition to the FENE potentials, bonded triplets interact through a bending potential, to simulate semiflexible polymers[56]:

$$U_{\mathrm{ang}}(\theta) = \frac{\epsilon_b}{2}[1-\cos(\theta)] \quad \text{(Equation 5)}$$

where $\theta$ is the triplet angle and $\epsilon_b = 2$ is the bending stiffness. The solvent is simulated implicitly using a Langevin thermostat.[57] The thermostat also ensures that the temperature $T$ is kept constant during the simulation at $T = 1$, which corresponds to 37 °C in this case. The viscous friction that each bead experiences is $\zeta = 10$. The simulations are carried out using the LAMMPS software,[49,58] and time integration is performed using the velocity Verlet algorithm, with time step $\delta t = 2 \times 10^{-3}$.

## Charge distribution of Ki-67 and RNA

To each bead comprising the RNA molecules, we assign the same negative charge $q_{\mathrm{RNA}} = -15$, so that RNA polymers are uniformly charged. The total charge of an RNA molecule $N_{\mathrm{RNA}}q_{\mathrm{RNA}} = -1500$. We have also performed simulations with $q_{\mathrm{RNA}} = -10$, finding the same qualitative results (not shown). The beads comprising the surfaces of the two chromosomes have a weak negative charge $q_{\mathrm{chr}} = -0.5$. The Ki-67 polymers are also uniformly charged (each bead having charge $q_{\mathrm{Ki67}}$), except for the fifth bead from the polymer's end, which is given a higher charge $q_{\mathrm{CP}}$. This mimics the charged patch (CP) experimentally observed in Ki-67 molecules. The charges $q_{\mathrm{Ki67}}$ and $q_{\mathrm{CP}}$ are chosen to mimic the charge state of Ki-67 during early mitosis at the start of the simulation (*i.e.*, at time $t = 0$). In particular, we consider the theoretical charge distribution of a Ki-67 molecule with 150 phosphorylated amino acids (thus adding a total charge of $-300$ in atomic units – see below for more details on how the theoretical distribution is calculated). Thus, the initial charge of the Ki-67 beads (excluding the CP) is $q_{\mathrm{Ki67}}(0) = -8.54$ and the initial charge of the CP is $q_{\mathrm{CP}}(0) = 6.17$ [total charge $Q_{\mathrm{Ki67}}(0) = 23q_{\mathrm{Ki67}} + q_{\mathrm{CP}} = -190.2$].

To simulate the gradual switching of Ki-67 from the phosphorylated to the dephosphorylated state, the charge of both the CP and of the rest of the chain is increased according to the following sigmoidal function:

$$q_\alpha(t) = q_\alpha(0) + \frac{q_\alpha(\infty) - q_\alpha(0)}{1+\exp\left(\frac{t_{\mathrm{tot}}/2 - t}{\tau}\right)} \quad (\alpha = \mathrm{Ki67}, \mathrm{CP}) \quad \text{(Equation 6)}$$

where $t_{\mathrm{tot}} = 6 \times 10^5$ is the total simulation in MD reduced units, and $\tau = 3 \times 10^4$ is a typical time for the change variation. With this choice, at the end of the simulation, the charge distribution of the Ki-67 molecules corresponds to the mitotic exit (fully dephosphorylated) state, *i.e.*, $q_{\mathrm{Ki67}}(t_{\mathrm{tot}}) \simeq q_{\mathrm{Ki67}}(\infty) = 3.73$ and $q_{\mathrm{CP}}(t_{\mathrm{tot}}) \simeq q_{\mathrm{CP}}(\infty) = 24.15$ [total charge $Q_{\mathrm{Ki67}}(\infty) = 109.8$].

## Measurement of force per unit area

To precisely quantify the force acting between the chromosomes, we perform simulations in which the Ki-67 molecules are grafted to surfaces, representing the surfaces of the chromosomes. As the focus of these simulations is not to study the formation of condensates of Ki-67 and RNA in solution, we do not include free (cytoplasmic) Ki-67 molecules. The two square surfaces (area $A = 4.9 \times 10^2$) are kept fixed in space at a constant distance $L_z = 30$ from each other, with the Ki-67 brushes facing each other. We graft to each surface 100 Ki-67 molecules (total number of Ki-67 molecules in the system $n_{\mathrm{Ki67}} = 200$), which are regularly arranged on a square lattice and bound to the surface by FENE bonds (Equation 4). The surface density of the grafted Ki-67 is $\rho_g = 2.0 \times 10^{-2}$ or approximately 140 $\mu\mathrm{m}^{-2}$ in experimental units. We additionally simulate $n_{\mathrm{RNA}} = 24$ free RNA polymers of length 100 in the space comprised between the two grafted surfaces. Periodic boundary conditions are applied in the $x$ and $y$ directions, which are parallel to the surfaces.

The system is equilibrated for a time of $10^5$ using only the excluded volume interactions before the production run with the full interactions. During production (duration $t_{\mathrm{tot}} = 6 \times 10^5$), the charge of the Ki-67 molecules is changed according to Equation 6 to model dephosphorylation. During the production run, we measure the $zz$-component of the stress tensor, $\sigma_{zz}$, evaluated using the *compute pressure* LAMMPS command. This quantity has the dimensions of pressure and corresponds to the force per unit area acting on the two surfaces. If its value is negative, there is an attractive force between the two surfaces; if it is positive, the force is repulsive. To assess the role of the CP in determining the strength of the interaction between the two surfaces, we additionally perform simulations in which the CP is completely removed (the Ki-67 polymer thus comprising 23 instead of 24 beads). For each set of parameters, we perform ten independent simulation runs (equilibration and production) and average the results over these simulations. In addition to these simulations, we also perform some in which RNA or Ki-67 is removed, in order to measure the force between the two surfaces in the absence of one of these two molecules. For these simulations, we performed five independent runs.

### Simulation of chromosome clustering

To model chromosome clustering triggered by the dephosphorylation of Ki-67 and mediated by RNA, we model the chromosome sections as rigid half cylinders with radius $R = 17.2$ and height $h = 30$. The two half cylinders face each other at the start of the simulation and are constrained to only undergo translational motion with respect to one another, along the $x$-axis of the box. The mass of the beads comprising the chromosomes is set to $m = 0.1$, so that the total mass of a chromosome is $M_{chr} = 185.5$. This is done in order to facilitate the movement of the chromosomes. A larger mass would lead qualitatively to the same dynamics but would require a longer simulation time to observe separation/clustering of the chromosomes. The simulations are carried out in a rectangular cuboid simulation box with edges $L_x = 120$ and $L_z = L_y = 75$, and periodic boundary conditions in all three spatial directions.

The Ki-67 brush is modeled by grafting $n_{Ki67} = 80$ bead-spring polymer chains of $N_{Ki67} = 24$ beads on the surface of the chromosomes. These chains are regularly arranged on a square lattice on the chromosomes' surface and bound to it by a finite extensible nonlinear elastic (FENE) bond. Cytoplasmic Ki-67 is modeled by $n^{free}_{Ki67} = 100$ identical bead-spring polymers (without the LR domain) which are not bound to the chromosomes' surface and are free to move in the simulation box. Due to the different geometry, for simplicity, we choose a slightly higher surface density of the grafted Ki-67 than the one used for the simulations with the fixed surfaces, namely $\rho_g = 2.5 \times 10^{-2}$, or approximately 170 $\mu m^{-2}$ in experimental units. Finally, we also model RNA as $n_{RNA} = 100$ bead-spring polymer chains of $N_{RNA} = 100$ beads (bead diameter = $\sigma$); the RNA molecules can also freely move in the simulation box. To investigate the role of RNA in chromosome clustering, we have also considered systems without RNA.

In order to study the effect of the Ki-67 charge distribution on the interaction between chromosomes, we initially placed them facing each other with their surfaces at a distance d = 26, slightly larger than the contour length of a Ki-67 molecule. The system is initially equilibrated for a time of $10^5$ using only the excluded volume interactions and with the two chromosomes held in place. Then, at time $t = 0$, we introduce the electrostatic interaction and simultaneously release the chromosomes, so that they are free to translate along the $x$-axis. During the simulation, which lasts a time $t_{tot} = 6 \times 10^5$, the charge of the Ki-67 beads evolves according to Equation 6. We perform five independent simulation runs (equilibration and production) and average the results over these simulations.

### Simulation of condensation in solution

To better display how Ki-67 and RNA cluster into condensates in simulations as Ki-67 is dephosphorylated, we perform additional simulations of Ki-67 and RNA molecules in solution. In these simulations, there are no surfaces representing the chromosomes, and thus no grafted Ki-67 molecules. We simulate $n^{free}_{Ki67} = 400$ Ki-67 molecules and $n_{RNA} = 100$ RNA molecules. The charge of Ki-67 is chosen to mimic the fully dephosphorylated state reached in mitotic exit. The total concentration (number of beads per unit volume) is $c = 10^{-2}$, and the simulations are performed in a cubic box (edges $L_x = L_y = L_z = 125.1$) with periodic boundary conditions in all spatial directions. The system is equilibrated for a time of $10^5$ using only the excluded volume interactions before the production run with the full interactions. (duration $t_{tot} = 2 \times 10^5$). For these simulations, we use a slightly larger time step, $\delta t = 5 \times 10^{-3}$ instead of $\delta t = 2 \times 10^{-3}$. As these simulations are performed to qualitatively show that Ki-67 and RNA cluster into condensates, and given that the simulated system is rather large, we performed a single simulation run.

### Charge prediction for simulations

Ki-67 protein sequence was split into 24 beads of $\simeq$ 120 amino acid residues per bead (Table S1), omitting the LR domain. The charge per bead (dephosphorylated) was calculated based on the amino acid sequence using a customized R script based on the net charge calculation of the 'seqinr' R package and pK values from EMBOSS considering a pH of 7. To estimate the bead charges in a phosphorylated state, we calculated the fraction of serine and threonine residues (potential phosphorylation sites) of Ki-67ΔLR located in the specific bead sequence and added the charge of the phosphorylation assuming a total of 150 phosphorylation sites and $-2$ net charge per phosphorylated residue to the charge of the dephosphorylated bead: ($-2 \times$ [fraction $S + T$] $\times$ 150 + bead charge[dephosphorylated]).

### Units conversion

To convert the simulation units into experimental ones (Table S2), we start with the observation that the brush height during early mitosis, measured as the average root-mean-squared end-to-end distance $[\langle R_e^2 \rangle]^{1/2}$, is $\simeq 7.3\sigma$ in the simulations. Experimentally, the brush height during early mitosis is approximately 90 nm. Thus, we set $\sigma = 90$ nm/7.3 $\simeq$ 12 nm. The grafting density of Ki-67 molecules in simulation units is $\rho_g = 2.5 \times 10^{-2}\sigma^{-2}$ (for the simulations with the two half cylinders), which corresponds to $\simeq$ 170 $\mu m^{-2}$ in experimental units. The unit charge $q_0 = (4\pi\epsilon_0\sigma\epsilon)^{1/2}$ can be estimated by setting $\epsilon$ (the unit of energy) to be equal to $k_BT$, with $k_B$ Boltzmann's constant and $T = 37$ °C $\simeq$ 310 K. In experimental units, $k_BT \simeq 4.3 \times 10^{-21}$ J. The unit charge is thus $q_0 \simeq 8.7 \times 10^{-20}$ C, which corresponds to $\simeq$ 0.55 atomic charge units. In accordance with the unit length conversion, we set the unit mass $m$ (mass of a bead of a Ki-67 polymer in the simulations) to be equal to 1/24th of the mass of a Ki-67 molecule, which is $3.58 \times 10^5$ Dalton = $5.96 \times 10^{-19}$ g. Thus, $m = 2.5 \times 10^{-20}$ g.

## QUANTIFICATION AND STATISTICAL ANALYSIS

Significance was tested relative to cells expressing full-length Ki-67 or untreated cells (Control) using two-tailed unpaired t test in Prism 10. Statistical tests, $p$ values, and number of replicates are indicated in the figure legends.

Detailed sample numbers:
Figures 1B–1F: n = 21 (Ki-67); n = 18 (Ki-67ΔLR); n = 31 (LR); n = 177 (KO).
Figure 2E: n = 21 (Ki-67); n = 28 (Ki-67(139E)); n = 23 (Ki-67(139D)).
Figures 2G and 2H: n = 23 (Ki-67ΔLR); n = 37 (Ki-67(139EΔLR)); n = 23 (Ki-67(139DΔLR)).
Figures 3C and 3D: n = 26 (ΔLR); n = 30 (C terminusΔLR); n = 33 (N terminus); n = 23 (N terminusΔCP); n = 29 (N terminusΔFASI).
Figure 3F: n = 23 (Ki-67); n = 19 (Ki-67ΔN terminus); n = 26 (Ki-67ΔRepeats); n = 26 (Ki-67ΔCP); n = 22 (Ki-67ΔFASI).
Figures 4D and 4E: n = 22 (N terminus); n = 19 (N terminus(CP(RK→A))); n = 26 (N terminusΔCP-strict).
Figure 4G: n = 27 (Ki-67); n = 39 (Ki-67(CP(RK→A))); n = 25 (Ki-67ΔCP-strict).
Figure 5H: Chromosome measurements before flavopiridol: n = 70 (Ki-67); n = 143 (Ki-67(139E)); n = 141(Ki-67(129E)). Chromosome measurements after flavopiridol: n = 29 (Ki-67); n = 97 (Ki-67(139E)); n = 90(Ki-67(129E)).
Figure 6B: n = 235 (metaphase KO); n = 109 (metaphase WT); n = 263 (anaphase KO); n = 193 (anaphase WT).
Figures 6D and 6E: n = 30 (Non-injected), n = n = 17 (Dextran-injected), n = 14 (RNase-injected).
Figures 6G–6J: n = 22 (Control); n = 26 (Amanitin); n = 52 (Act D).